1 **Detection of Orsay viral replication intermediates reveals spatial and regulatory links to**

2 ***Caenorhabditis elegans* innate immune responses**

3 Supraja Ranganathan, P. Joseph Aruscavage, Brenda L. Bass

4 Department of Biochemistry, University of Utah, Salt Lake City, Utah, USA 84112-5650

5 **Short title:** Viral replication intermediates in *C. elegans*

Abstract

For a positive-strand RNA virus, the encoded viral RNA-dependent RNA polymerase (oRdRP) synthesizes complementary antigenome strand and uses it as a template for amplifying the viral genome, generating various replication intermediates. Structural proteins and viral genome are packaged into virions, but the fate of replication intermediates is underexplored. Here, we investigate Orsay Virus (OV) replication intermediates, including antigenome, oRdRP and double stranded RNA (dsRNA), using PCR and fluorescence-based imaging in *C. elegans* intestines. As for other positive-strand RNA viruses, we find that genome is in vast excess of antigenome. Antigenome is only visualized in cells when using denaturation protocols, indicating basepaired intermediates. OV antigenome is observed with distinct cytoplasmic and perinuclear localization patterns that depend on factors required for generation of primary, but not secondary, siRNAs. In both wildtype and RNA interference (RNAi) mutants, viral dsRNA is observed in the cytoplasm associated with oRdRP, suggesting cytoplasmic virus replication hubs. Additionally, using antibodies to oRdRP, we observed spherical structures of ~1μm in diameter defined by oRdRP at their surface; over 75% of infected wildtype animals show these structures, which associate with mitochondria and autophagosomes in an antiviral RNAi- and autophagy-dependent manner, respectively. Our study defines new features of OV replication intermediates in wildtype animals, setting the stage for understanding their connection to the viral life cycle and host antiviral pathways.

Author Summary

Viruses infect and cause disease in all organisms. Once they enter an organism, or host, viruses make copies of themselves in a process called replication, and this process generates byproducts that are recognized as foreign by the host. This signals the host to begin protecting itself using pathways such as the innate immune response, underscoring the importance of understanding where and when replication byproducts are generated. Here we utilize *Caenorhabditis elegans*, a microscopic roundworm, to detect the viral replication intermediates of its naturally infecting pathogen, Orsay Virus (OV). For the first time, we detect OV antigenome, a byproduct that is used as a template for viral genome replication. We report a previously uncharacterized antigenome-containing perinuclear granule

33 that is partially dependent on the antiviral RNA interference (RNAi) pathway, an invertebrate immune
34 response. We also identify regions of cytoplasmic viral replication and unusually large (~1 micron)
35 spherical structures lined with the viral RNA-dependent RNA polymerase, an enzyme made by the virus
36 for its replication. By characterizing important viral replication byproducts, our studies set the stage for
37 understanding mechanistic connections between viral infection and the host response.

38 **Introduction**

39 Orsay Virus (OV) is a naturally-infecting *C. elegans* pathogen that closely resembles the
40 *Nodaviridae* family of viruses. OV is a positive strand, single-stranded RNA (+ssRNA) virus, with a
41 bipartite genome (oRNA1 and oRNA2) that preferentially infects *C. elegans* intestinal cells where it is
42 predominantly restricted to anterior cells [1–3]. oRNA1 encodes an RNA-dependent RNA Polymerase
43 (oRdRP), and oRNA2 encodes the capsid, δ (delta), and capsid-δ fusion proteins [4].

44 While details of OV replication and its intermediates are just emerging [3,5], it can be presumed
45 that general features of positive-strand RNA viruses are operative [6,7]. Replication of a positive-strand
46 RNA virus begins with translation of its RdRP from the genomic strand. The RdRP first synthesizes a
47 complementary strand to the genome, the antigenome (-ssRNA), and this is the first RNA replication
48 intermediate. The antigenome is then used as a template by the RdRP to amplify the viral genome [8].
49 The perfectly complementary strands of genome and antigenome can basepair to form a viral double-
50 stranded RNA (dsRNA), another RNA intermediate of viral replication. Replication of closely related
51 nodaviruses occurs inside membrane-enclosed compartments that protect viral RNA and other
52 replication intermediates from the host antiviral machinery [7]. The structural proteins along with the
53 viral genome they encapsulate are packaged and processed into a mature virion that is then egressed
54 out of the cell.

55 Some viral replication intermediates are recognized by helicases to elicit an antiviral response.
56 Among vertebrates, the RIG-I-like Receptor (RLR) family of helicases recognize dsRNA to elicit an
57 interferon response. Invertebrates do not have interferon pathways, and invertebrates such as *C.*
58 *elegans* instead utilize RNA interference (RNAi). In RNAi it is the enzyme Dicer that recognizes dsRNA,
59 using a helicase domain related to that of RLRs. *C. elegans* Dicer (DCR-1) forms an antiviral RNAi
60 complex with DRH-1, a Dicer-related helicase and RLR ortholog, and RDE-4 (RNAi-DEficient 4), a
61 dsRNA binding protein. This antiviral complex cleaves viral dsRNA into 23H (H=A,U,C>G at 5' end)
62 primary small-interfering RNAs (1° siRNAs). The 1° siRNA is then bound by RDE-1 (RNAi-deficient 1),
63 an argonaute protein, and passed to other factors for generation and amplification of 22G (preferentially
64 G at 5' end) secondary siRNAs (2° siRNAs) that are complementary to the viral genome [9,10].

65 The *C. elegans* antiviral response also involves OV-induced genes (OVIGs) [2,11], a subset of
66 which are also the Intracellular Pathogen Response (IPR) genes [12], a transcriptional response
67 somewhat analogous to the mammalian interferon response, and this requires DRH-1, but not DCR-1
68 or RDE-4 [13]. DRH-1-mediated OVIG induction occurs after viral replication, but the exact viral
69 intermediate that DRH-1 recognizes to trigger OVIGs is unknown. However, recently OV dsRNA was
70 visualized in association with DRH-1 in *C. elegans* intestines, raising the possibility that this recognition
71 is important for triggering OVIGs [5]. *C. elegans* lacking RNAi factors have increased sensitivity to OV,
72 and these mutant strains are widely used to understand OV replication dynamics and downstream
73 RNAi responses [3]. Given that replication is required to elicit host antiviral responses, it is important to
74 understand the temporal and spatial organization of replication intermediates. The predominantly
75 studied viral replication byproduct is viral dsRNA; other replication intermediates are often ignored
76 leading to an incomplete picture of replication dynamics and antiviral responses, especially in a
77 wildtype background.
78 Here we detect and characterize three replication intermediates, oRdRP, oRNA1 antigenome,
79 and OV dsRNA, in both wildtype and RNAi mutant backgrounds, capturing key steps of viral replication
80 and their spatial organization. We show that OV is like other +ssRNA viruses in that the viral genomic
81 strand is present in vast abundance relative to the antigenomic strand, in both wildtype and RNAi
82 mutants. Using single molecule FISH (smFISH), we show that the OV antigenome is detectible in cells
83 with genomic strand, and detection is facilitated with denaturation protocols, indicating most
84 antigenome is basepaired. Unexpectedly, we observed antigenomic RNA within perinuclear regions that
85 are partially depleted in strains defective for primary siRNA biogenesis, but not those aberrant for
86 secondary siRNA amplification, setting the stage for connecting OV infection and replication with the
87 downstream antiviral RNAi pathway. Surprisingly, we did not detect RNAi factors associating with the
88 perinuclear-localized antigenome. We observed oRdRP-associated dsRNA puncta revealing possible
89 replication hubs. Infected wildtype intestinal cells also showed oRdRP in lumen-containing spherical
90 structures of ~1μm in diameter, in association with both mitochondria and autophagosomes, and
91 dependent on antiviral RNAi and autophagy pathways. Together, the results reveal new hubs of viral

92 replication and processing and emphasize the importance of detecting and understanding viral
93 replication in a wildtype background.

94 **Results**

95 **OV genomic strand accumulates significantly more than antigenomic strand in wildtype and**
96 **RNAi mutants**

97 OV infection in *C. elegans* is typically measured by RT-qPCR in a strand-agnostic manner and
98 denoted as viral load, or by monitoring genomic strand accumulation using northern blot analysis. For a
99 plus-strand virus such as OV, these methods largely reflect levels of the more abundant genome but
100 offer little information about the less abundant antigenome [1]. To acquire this information, we first
101 monitored OV-infected animals with strand-specific RT-qPCR. We designed strand-specific probes for
102 oRNA1 genome or antigenome that each included a unique flanking sequence so that strand-specific
103 complementary DNA (cDNA) could be quantified with qPCR, using the unique flanking region as a
104 primer and a second downstream on the respective oRNA1 strand (**Fig 1A**). We also performed
105 northern blot analysis to complement our strand-specific RT-qPCR method and directly detect viral RNA
106 abundance.

107 We in vitro transcribed and purified fragments of genomic and antigenomic strands of oRNA1,
108 each ~500 nucleotides (nts) long, and used these transcripts to generate standard curves for
109 quantifying copy number in a strand-specific manner (**S1A and S1B Figs**); these transcripts were also
110 used to confirm that antigenomic probes were specific and able to detect 10^6 copies of purified ~500nt
111 antigenome ssRNA by northern blot assay (**S1C Fig)**. We then monitored appearance of genome and
112 antigenome over time, using two infection protocols: one monitoring infection of L3 larvae at 12- and
113 24-hours post infection (hpi; **Fig 1B**), and a second aimed at quantifying strands after prolonged
114 infection, by infecting L1 larvae and assaying 48 and 72hpi (**Fig 1C**). For the latter, we chose infection
115 times that maintained animals in the same reproductive cycle (72hpi) so that populations would not be
116 contaminated with newly hatched larvae.

117 For each protocol, we compared infection of wildtype (N2) animals to that observed in antiviral
118 RNAi mutants, *drh-1(uu60), rde-4(uu71), rde-1(ne219)*, and a helicase point mutant (G492R*)* of DCR-1

119 (*eri-4(mg375)*) [14,15], referred to here as *dcr-1(mg375)* (**Figs 1D and 1E**). We observed significantly
120 higher levels of genome than antigenome for wildtype and RNAi mutant strains. Further, for each
121 infection protocol, with few exceptions, we observed a dramatic and significant increase in oRNA1
122 genome copy numbers at 24hpi and 72hpi relative to 12hpi or 48hpi, respectively, in both wildtype and
123 mutant animals. We observed a modest increase in oRNA1 antigenome relative to wildtype in *drh-1,*
124 *rde-4* or *rde-1* mutants, but at early time points this was not observed in *dcr-1(mg375)* mutants (**Figs**
125 **1D and 1E; points relative to pink dotted line**). Quantification showed greater than 100-fold increase
126 in genome over antigenome at 12hpi, and over 1000-fold increase at all other infection times, for both
127 wildtype and RNAi mutants (**S1D and S1E Figs**). Northern blot analyses confirmed the low levels of
128 antigenome compared to genome (**S1F and S1G Figs**); controls established that if present antigenome
129 could be detected, but oRNA1 antigenome was below the limit of detection for wildtype and RNAi
130 mutants at all time points tested (12-72 hpi). oRNA1 genome was first detected at 24hpi for RNAi
131 mutants, and increased over time, but was only faintly detected at 72hpi for wildtype strains.

132 Consistently, levels of genomic RNA were higher in RNAi mutants than wildtype (**Figs 1D and**
133 **1E**), and trends matched the increase in viral load as determined in a strand-agnostic manner,
134 consistent with prior studies [10,13] (**S1H and S1I Figs).** In accordance with published studies, we
135 observed that the antiviral RNAi mutants, *drh-1*, *rde-4* and *rde-1*, were sensitive to OV and showed
136 increased viral load relative to wildtype at all timepoints tested, by all methods [10]. While previous
137 studies have reported the sensitivity of *dcr-1* using deletion mutants or knockdown (RNAi) [10,13], we
138 report the involvement of the helicase domain of DCR-1. The helicase mutant *dcr-1(mg375)* showed a
139 delayed response with a moderate increase in viral load, ~10-fold at 12hpi and 24hpi, and ~100-fold at
140 48hpi and 72hpi **(Figs 1D, 1E, S1H and S1I)**.

141 Prior studies have looked at viral infection in the constitutively infected JU1580 strain, which has
142 a mutation in DRH-1 and is highly sensitive to OV infection [1,4]. To connect our studies to prior studies
143 we showed that a high viral load in the JU1580 strain relative to wildtype, as determined using strand-
144 agnostic protocols, correlated with a robust accumulation of oRNA1 genomic strand by both strand-
145 specific RT-qPCR and northern blot, while the oRNA1 antigenome levels remained significantly lower,

146 ~1300-fold, (*p-value<0.0001*) (**Figs 1F, S1F and S1G**). This emphasizes that the antigenomic strand is
147 much lower than the genomic strand even with constitutive infection. To test if the ratio of genome to
148 antigenome was a property inherent to oRdRP mediated replication, we also monitored a heat shock-
149 inducible replicon system expressing wildtype ($oRdRP^{WT}$) or a replication-incompetent mutant
150 ($oRdRP^{mut}$) oRNA1 [16]. In the complete absence of infection, we observed a significant increase in
151 genome and antigenome upon inducing the expression of $oRdRP^{WT}$ but not $oRdRP^{mut}$, and notably,
152 antigenome levels remained significantly lower (**Fig 1G**), which was confirmed by northern blot (**S1F**
153 **Fig**).

154 In summary, these studies indicate that the increase in viral load commonly measured using
155 strand-agnostic methods largely reflects an increase in genomic strand. At the time points tested, for
156 wildtype and RNAi mutant strains, we found that the genomic strand, the strand that is packaged into
157 virions, is in far excess of the antigenomic strand, which is only an intermediate, and these ratios are
158 intrinsic to the oRdRP and its tight regulation by host factors [17,18].

159 **oRNA1 antigenome is visualized only with conditions that denature RNA basepairs**

160 To gain insight into the localization pattern of OV genome and antigenome within infected cells, we
161 performed smFISH analyses by designing multiple strand-specific fluorescent deoxyoligonucleotide
162 probes for oRNA1 (27 probes, genomic strand; 48 probes, antigenomic strand). For initial optimization
163 of the protocol, we used OV infection-sensitive *jyIs8;rde-1* animals. *jyIs8* contains an integrated
164 transgene that expresses GFP under the control of the promoter of an OVIG, *pals-5*, and was used as
165 a marker for infection [19]. Uninfected controls established the absence of signal for *pals-5p::GFP* and
166 oRNA1 strands, while as in prior studies [19], a strong signal in the pharynx (asterisk) in the same
167 channel as antigenome was observed from fluorescence of the *myo-2p::mCherry* marker included in
168 the *jyIs8* transgene (**Fig 2A; uninfected**). At 24hpi we saw robust GFP expression in multiple intestinal
169 cells that typically extended beyond the cell(s) with abundant accumulation of oRNA1 genome. The
170 multi-cell GFP expression is consistent with prior studies showing distribution of DRH-1 and ZIP-1
171 beyond infected cells [5,20]. In these OV genome-containing intestinal cells, we observed ~95% of
172 infected animals had a diffuse cytoplasmic signal of antigenome without distinct puncta (**Figs 2A,**

173 **infected (-) denature and 2B**). We hypothesized that antigenome might be hybridized to the genome,
174 forming the viral dsRNA often observed during viral infection. To test this, we treated animals with
175 50mM NaOH for ~30 seconds to promote dsRNA denaturation prior to hybridization [21], hereafter
176 referred to as denature-smFISH (dsmFISH). Indeed, after denaturation we observed ~97% of infected
177 animals with oRNA1 antigenome punctate signal (**Figs 2A, infected (+) denature and 2B**). This
178 indicated that most of the oRNA1 antigenome was either basepaired with the genome or had extensive
179 intramolecular secondary structure. We used the dsmFISH denaturing conditions for subsequent
180 experiments.

181 Since the diffuse cytoplasmic signal observed using probes to the antigenome was similar to the
182 pattern of the oRNA1 genome signal, and because we anticipated that antigenome, as for other
183 positive-strand RNA viruses [7,22,23], would be localized to discrete replication compartments, we
184 considered the possibility that the diffuse antigenome signal was a consequence of bleed though from
185 the genome channel. Thus, we monitored antigenome in infected animals that had not been probed for
186 genome, and vice-versa (**Figs 2C and 2D)**. We observed the diffuse signal in the antigenome channel
187 even when we only probed for genome, indicating bleed-through. In subsequent experiments we
188 considered the diffuse cytoplasmic signal as nonspecific background. However, a lower level of
189 cytoplasmic signal, and importantly, distinct puncta, were specific to antigenomic probes (**Fig 2C, white**
190 **arrowhead**).

191 **oRNA1 antigenome localizes to perinuclear foci upon infection**

192 We focused on the understudied antigenomic strand and its distribution during OV infection. At
193 24hpi, in both *jyIs8* (wildtype) and *jyIs8;rde-1* mutant backgrounds, we observed infected intestinal cells
194 with robust genome signal as well as distinct antigenome puncta (**Fig 3A**). We observed that *rde-1*
195 mutants exhibited more infected cells than wildtype as quantified by cytoplasmic genome signal (**Fig**
196 **3B**). Strikingly, we observed a distinct perinuclear localization of antigenomic RNA, emphasized by line
197 scan analysis, in both wildtype and *rde-1* mutant strains (**Fig 3A**). Quantification showed that in
198 wildtype or *rde-1* mutant strains, ~83% or ~78% of infected animals exhibited perinuclear localization,
199 respectively (**Fig 3C**). The perinuclear antigenome puncta lacked an obvious colocalizing genome

200 signal, but the line scan showed a peak of genomic signal closely associated (**Figs 3D and 3E**). While
201 the perinuclear antigenome puncta was the most common pattern observed, multiple biological
202 replicates (≥10) revealed other patterns in wildtype infected animals (**Figs 3F-J**). For example, close
203 association of antigenomic puncta with genome was observed in the cytoplasm (**Figs 3F and 3G**). In
204 other cases, antigenomic RNA was observed as concentrated cytoplasmic foci surrounded by genome
205 signal (**Figs 3H, white arrowhead and 3I**). Given that antigenomic strand is used as a template for
206 viral replication to generate viral genome, possibly the closely associated genome and concentrated
207 antigenome puncta could indicate active replication hubs in the infected cytoplasm. However, in
208 infected animals that only exhibited genomic signal in the lumen **(Fig 3J**), as expected in animals that
209 have released the packaged virions [2], we did not observe any cells with antigenomic signal, indicating
210 antigenomic strands may be degraded, processed through efficient antiviral defense mechanisms, or
211 below limits of detection. These studies allowed the first visualization of the antigenomic strand in OV-
212 infected *C. elegans* and also revealed its distinct localization patterns.

213 **Primary siRNA biogenesis, but not secondary siRNA amplification, is partially required for**
214 **perinuclear localization of antigenome**

215 A key aspect of antiviral defense in *C. elegans* is cleavage of viral dsRNA by the antiviral
216 complex, comprised of DCR-1, DRH-1, and RDE-4 [24]. The antiviral complex processes viral dsRNA
217 to produce 1° (23H) siRNAs [25], which are bound by RDE-1 for presentation to 2° (22G) siRNA
218 amplification factors. Mutations or deletions in DCR-1, DRH-1 or RDE-4 prevent accumulation of both
219 1° and 2° siRNAs, while RDE-1 mutants accumulate primary siRNAs but lack secondary siRNAs [10].
220 Given the key role of these RNAi factors in antiviral defense, we wondered about their relationship to
221 OV replication intermediates. We infected synchronized L1 larvae of RNAi mutants, *dcr-1(mg375), drh-*
222 *1(uu60), rde-4(uu71), rde-1(ne219)*, as well as wildtype (*N2*), for 24 hours and performed dsmFISH. As
223 observed previously (**Fig 2A, uninfected**), a minimal background of diffuse fluorescence in the
224 antigenome channel in uninfected animals was observed for all strains (**S2 Fig**). At 24hpi, both wildtype
225 and RNAi mutants showed abundant genome signal in one or more intestinal cells, with significantly
226 more infected cells in RNAi mutants (**Figs 4A, G+AG column 1, and 4B**). Consistent with our previous

227 experiments, we observed distinct perinuclear localization of antigenome in wildtype (~81% animals) or
228 *rde-1* mutants (~83% animals) (**Figs 4A and 4C, *N2, rde-1***). In antiviral RNAi mutant animals, we
229 observed a partial reduction in animals exhibiting perinuclear localization of antigenome (**Figs 4A and**
230 **4C, *dcr-1, drh-1, rde-4***). While antiviral RNAi mutants cannot process viral dsRNA as efficiently as
231 wildtype, some non-processive activity remains, as evidenced by siRNA reads that map to ends of the
232 viral genome/antigenome [10,26]. Possibly the partial reduction in perinuclear puncta relates to this
233 incomplete loss of activity. MUT-16 is a scaffolding component required for mutator foci formation in the
234 germline, sites where secondary siRNA amplification occurs [27,28]. MUT-16 is also required for
235 secondary siRNA amplification during OV infection [29]. We used a *mut-16(pk710)* strain to test if this
236 strain phenocopies *rde-1* mutants with respect to perinuclear localization. We observed that over 85%
237 of infected *mut-16* mutants at 24hpi exhibited perinuclear localization of antigenome, not significantly
238 different from wildtype or *rde-1* mutant backgrounds (**Figs 4A and 4C, *mut-16***). Since *rde-1* or *mut-16*
239 mutant animals, which accumulate 1° siRNAs but lack 2° siRNAs, show robust perinuclear localization
240 of antigenome, our experiments suggest perinuclear localization of the antigenome requires wildtype
241 accumulation of 1° siRNAs but is unaffected by aberrant accumulation of 2° siRNAs. Together these
242 results indicate that the signal from the perinuclear-localized antigenome in some way depends on
243 proper function of the three factors of the antiviral RNAi complex.

244 **OV antigenome perinuclear puncta do not colocalize with antiviral RNAi factors**

245 Given the partial loss of perinuclear antigenome signal in animals with deficiencies in the antiviral
246 complex, we considered the possibility that factors of the antiviral RNAi pathway (**Fig 5A**) might colocalize
247 with the perinuclear antigenome signal. We took advantage of existing strains for DCR-1, RDE-1 and
248 DRH-3, a helicase related to DRH-1 that is involved in 2° siRNA amplification, that were tagged at the
249 endogenous locus with 3XFLAG::GFP. We observed a diffuse distribution of DCR-1, RDE-1 and DRH-3
250 without infection (**Figs 5B, 5C and 5D**). As expected from prior studies [28], in uninfected and infected
251 animals we observed DRH-3 localized at perinuclear foci in the germline which served as an internal
252 control (**Fig 5D**).

253 For all GFP-tagged proteins, DCR-1, RDE-1 and DRH-3, at 24hpi we observed distinct
254 cytoplasmic puncta in cells with genomic signal (**Figs 5E, 5G and 5H**), and these puncta were clearly
255 separated from perinuclear antigenome puncta, as confirmed by line scan for DCR-1 (**Figs 5E and 5F**).
256 Notably, DRH-1, a known interactor of DCR-1, also exhibits cytoplasmic punctate distribution in OV
257 infected cells [5]. The pattern for DCR-1 was observed in 100% of infected animals, and for RDE-1 and
258 DRH-3, in around 50% of infected animals. Thus, although we observed that mutations in factors
259 involved in the production of 1° siRNAs, but not those required for 2° siRNA amplification, showed
260 reduced number of infected animals with perinuclear antigenome (**Fig 4C**), at least for the factors
261 tested, we do not observe the factors themselves localizing to the perinuclear region.

262 **dsRNA accumulates during OV infection and associates with oRdRP**

263 Positive-strand viruses amplify their genome using the antigenome as template [8], and viral
264 dsRNA arises during this process. dsRNA is often visualized using dsRNA-specific antibodies [30], and
265 to understand if dsRNA accumulation varies in wildtype and RNAi mutants, we used the J2 dsRNA-
266 specific antibody with a dot blot assay, first showing that we could detect as low as 50pg of purified 800
267 basepair dsRNA (**S3 Fig**). We then collected total RNA from OV-infected (72hpi) and uninfected
268 samples and again used the dot blot assay to monitor dsRNA accumulation. Control experiments
269 showed that dsRNA was not detected without OV infection, and consistent with the fact that wildtype
270 animals have efficient antiviral RNAi, we also did not observe dsRNA accumulation in wildtype animals
271 (**Fig 6A**); however, given the limited sensitivity of this assay, we cannot rule out the existence of low
272 levels of dsRNA in the wildtype background. Importantly, we detected dsRNA accumulation in all RNAi
273 mutants tested (**Fig 6A**).

274 To evaluate whether the dsRNA signal was from viral or endogenous dsRNA, we looked for oRdRP
275 colocalized with dsRNA in infected cells. We infected *jyIs8* (wildtype) or *jyIs8;rde-1* animals, picked
276 GFP-positive infected animals and performed intestinal immunofluorescence assays using antibodies
277 against oRdRP and dsRNA (J2). We observed that *pals-5p::GFP* expressing infected intestinal cells
278 showed both oRdRP and dsRNA puncta, colocalized, in both *jyIs8* and *jyIs8;rde-1* animals (**Fig 6B; red**
279 **arrowhead**). We also observed a strong nuclear dsRNA signal in oRdRP containing *pals-5::GFP*

280 expressing *jyIs8* intestinal cells that was not observed in uninfected animals or *jyIs8;rde-1* mutants (**Fig**
281 **6B, merge zoom**). The dsRNA that is colocalized with oRdRP is consistent with viral dsRNA being
282 produced during replication, while the nuclear dsRNA more likely reflects endogenous intronic dsRNA
283 induced in infected animals [25,31].

284 Interestingly, apart from oRdRP puncta, we noticed distinct oRdRP-containing spherical structures
285 in the *pals-5p::GFP* positive intestinal cells (**Fig 6B, merge zoom, white arrowhead**). Over 75% of
286 *pals-5p::GFP* positive wildtype animals exhibited at least one spherical oRdRP signal, with the rest only
287 showing RdRP puncta (*p=0.0046*); less than 50% of *rde-1* mutant animals exhibited oRdRP spheres.
288 We quantified the total number of oRdRP spheres per animal and observed that wildtype animals
289 showed between 5 to 58 spheres with an average diameter of 1.023μm (**Figs 6C and 6D)**. The number
290 of spheres per animal was significantly lower in *jyIs8;rde-1* animals (*p=0.0424)*, with 0 to 25 spheres
291 per animal and an average diameter of 1.122μm (*p=0.0154*), slightly higher than the observed diameter
292 in wildtype animals. While we did not observe any dsRNA puncta inside the oRdRP spherical
293 structures, we did find a few spheres closely associated with dsRNA puncta (**Fig 6B, merge zoom,**
294 **yellow arrowhead**).

295 **oRdRP spherical structures associate with mitochondria and autophagosomes**

296 Given that the oRdRP signal was present at the periphery of the spheres, we predicted that oRdRP,
297 similar to other *Nodaviridae* RdRPs [32], has transmembrane domains. We utilized four different
298 transmembrane domain prediction programs [33–37] and observed two distinct N-terminal
299 transmembrane domains, suggesting oRdRP is associated with membranes in infected cells (**S4 Fig)**.

300 To understand the nature of the spheres, we first tested whether the spheres associated with lipid
301 droplets. In *C. elegans* intestines, lipid droplets are ~1μm in diameter with a phospholipid monolayer
302 [38,39]. Using a neutral lipid stain, we observed a reduction in the number of lipid droplets in infected
303 intestines at 24hpi, relative to uninfected controls, consistent with other studies in the literature (**S5 Fig**)
304 [1,40]. However, while we observed lumen-containing oRdRP spheres in infected intestines, we did not
305 observe lipid stain within lumens, indicating that oRdRP does not associate with the membrane of lipid
306 droplets.

307 The *Nodaviridae* family of viruses utilize mitochondrial membranes to form compartments that aid in
308 replication [7,23]. To test whether oRdRP spheres were mitochondrial associated, we infected strains
309 containing the inner membrane protein *timm-50* tagged with *wrmScarlet* [41] and performed
310 immunofluorescence using oRdRP antibody at 24hpi. In infected intestinal cells, we observed distinct
311 oRdRP along with closely associated *wrmScarlet::timm-50* signal, also confirmed by line scan analysis,
312 consistent with an association of oRdRP spheres with mitochondrial membrane (**Figs 7A, 7B**).
313 Since oRdRP does not get packaged into virions, it seemed possible that oRdRP spheres
314 associated with autophagosomes as part of their degradation. Autophagosomes are multi-membrane
315 structures that are induced during autophagy, a degradation pathway for organelle turnover, as well as
316 for clearing viruses and viral proteins [42,43]. An important step of this degradation pathway is the
317 formation of spherical autophagosomes mediated by ATG-3 [44,45]. ATG-3 also plays a role in OV
318 infection at a step downstream of replication [46]. To test if the formation of oRdRP spheres is
319 dependent on ATG-3 we used the *atg-3(bp412)* mutant. At 24hpi, we observed significantly fewer
320 oRdRP spheres per infected animal, relative to wildtype (**Fig 7C**), phenocopying results from *rde-1*
321 mutants (**Fig 6B**). This is consistent with a connection between oRdRP spheres and the autophagy
322 pathway.
323 We then wanted to test whether the oRdRP spheres were themselves autophagosomes. We
324 utilized an intestinal autophagy flux reporter that expresses *GFP::LGG-1::mKate2* to mark
325 autophagosomes by the presence of *GFP::LGG-1* and absence of mKate2 [44]. Without infection, we
326 did not observe oRdRP staining but saw multiple *GFP+/mKate2-* puncta in *C. elegans* intestines,
327 indicating autophagosome formation (**Fig 7D, uninfected**). We chose a GFP+ punctum at random and
328 showed with a line scan a clear GFP signal, but no oRdRP signal in uninfected intestines (**Fig 7E, top**
329 **panel**). At 24hpi we observed abundant GFP+/mKate2- puncta, consistent with previous studies [19],
330 and lumen-containing oRdRP spheres in intestines (**Fig 7D, OV infected**). Using line scans and
331 quantification, we observed that ~50% of oRdRP spheres contained GFP signal in their lumen (**Fig 7E,**
332 **bottom panels, a**), while remaining spheres lacked this signal (**Fig 7E, bottom panels, b**). There were
333 also GFP::LGG-1 puncta that were not associated with oRdRP signal (**Fig 7E, OV infected, white**

334 **arrowhead**). Thus, a portion of oRdRP spheres are associated with autophagosomes, possibly
335 containing oRdRP destined for degradation, but as yet, the reason for the unique spherical structures is
336 unclear.

337 **Discussion**

338 The abnormal morphology of the intestine in RNAi mutant *C. elegans* after infection with OV has
339 been visualized with transmission electron microscopy [1], and the OV genome and oRdRP have been
340 visualized using smFISH and immunofluorescence [2,3]. Here we add to this understanding by
341 characterizing three OV replication intermediates: oRdRP, the antigenome, and dsRNA (**Fig 8**). Using
342 quantitative, strand-specific methods, we demonstrate that genome is in vast excess of antigenome
343 (**Fig 1**), as found in other positive-strand RNA viruses [1,21,47–49]. By utilizing a helicase mutant of
344 DCR-1 (*dcr-1(mg375)*), we confirm the importance of helicase function to antiviral RNAi and efficient
345 antiviral defense (**Figs 1 and S1**), as suggested previously with in vitro experiments [24]. By applying
346 denaturation protocols, we visualize the lowly abundant antigenome in intestinal cells (**Fig 2**), observing
347 both cytoplasmic and perinuclear localization (**Figs 3D-J**), with the latter affected by deficiencies in
348 factors that affect generation of 1°, but not 2°, siRNAs (**Fig 4**). While genomic RNA was not observed to
349 localize in the perinuclear region, it exhibited close association with the antigenome (**Fig 3**). The closely
350 associated genome-antigenome puncta in the cytoplasm possibly indicate replication hubs, as does the
351 observation of oRdRP associating with dsRNA puncta in the cytoplasm of infected cells (**Fig 6B**).
352 Notably, in wildtype animals, we also observed oRdRP at the surface of lumen-containing spheres, and
353 a decrease in the number of spheres in autophagy mutants suggests spheres may be related to host
354 clearance of viral byproducts (**Figs 6B and 7C-7E**). Our study offers an example of an invertebrate viral
355 infection model and sets the stage for a more complete spatial and temporal understanding of the OV
356 life cycle.

357 **Intercellular communication during OV infection**

358 In vertebrates, viral infection triggers the production and extracellular release of interferons,
359 which bind to cell surface receptors of neighboring cells to activate intracellular kinases that
360 phosphorylate STAT transcription factors, leading to their dimerization and translocation to the nucleus

361 where they induce transcription of Interferon Stimulated Genes (ISGs) to elicit antiviral defense [50,51].
362 In our studies of the invertebrate *C. elegans*, we also observed an intercellular response, whereby cells
363 that did not contain viral RNA but were proximal to those that did, showed expression of *pals-5*, a
364 member of the OVIGs, whose transcription is induced by OV infection (**Figs 2A and 3A**). *sta-1*, an
365 ortholog of mammalian STATs, also plays a role in OV infection by regulating the expression of antiviral
366 genes [52]. While DRH-1 and ZIP-1 have been observed to be activated in neighboring cells [5,20], we
367 speculate that, as for STATs in mammalian cells, *sta-1* may also be activated in neighboring cells to
368 regulate OVIGs, thereby conferring resistance to OV infection in these cells.

369 **Why is the antigenome localized to the perinuclear region?**

370 During infection, the antigenome is typically restricted to regions of viral replication [53].
371 Surprisingly, using dsmFISH, we observed ~80% of OV-infected wildtype animals with perinuclear
372 localized antigenome, without the presence of other signatures of replication, such as oRdRP, genome,
373 or dsRNA (**Figs 3A and 6B**). In the *C. elegans* germline, perinuclear regions are hubs for RNAi
374 machinery [28,54], but so far, such perinuclear granules have not been observed in somatic tissues.
375 However, given the overlap of factors observed in germline perinuclear puncta and those involved in
376 antiviral RNAi [27,28,55], it is perhaps not surprising that we observed a connection of the intestinal
377 perinuclear-localized antigenome and the antiviral RNAi pathway. Specifically, we observed a decrease
378 in the percentage of infected worms with perinuclear-localized antigenome in animals with deficiencies
379 in factors of the antiviral complex, known to affect levels of 1° siRNAs (DCR-1, DRH-1, RDE-4) (**Fig 4**).
380 Although the antiviral complex is necessary for efficient antiviral defense [24], mutations of *drh-1* or *rde-*
381 *4* typically do not completely eliminate production of 1° siRNAs [10]. For example, mutations in *drh-1*
382 often show siRNAs at the termini of the genome and antigenome, with loss of internal siRNAs,
383 consistent with a loss of processive cleavage [10,26]. So, the partial reduction in antigenome
384 perinuclear localization could be due to the diminished siRNA production of these mutant animals. By
385 contrast, animals with deficiencies in antiviral RNAi factors that affect levels of 2° siRNAs (RDE-1,
386 MUT-16) showed wildtype levels of perinuclear localized antigenome (**Fig 4**); this is noteworthy given

387 that MUT-16, a scaffolding protein, is required for mutator foci formation, a perinuclear granule in the
388 germline [28].

389 We also did not observe the factors themselves, DCR-1 or RDE-1 (**Figs 5E-H**) localized in the
390 perinuclear region, suggesting that the perinuclear puncta are not hubs for generation of siRNAs.
391 Consistent with previous reports [28], we also observed that DRH-3, required for 2° siRNA
392 amplification, did not localize to perinuclear foci in infected intestinal cells even with OV infection (**Fig**
393 **5H**). There are other factors involved in steps in between RDE-1 loading and 2° siRNA amplification,
394 such as RDE-8 [55], and also in the subsequent targeting of the genome for degradation, which
395 requires SAGO-2 [56]; it remains possible that these factors or others will be associated with the
396 perinuclear antigenome.

397 As evident from our strand-specific RT-qPCR assays, we observed a moderate increase in the
398 antigenomic strand abundance in RNAi mutants relative to WT (**Figs 1D and 1E**). Thus, it is also
399 possible that the loss of antigenomic perinuclear signal in primary RNAi mutants might correlate with an
400 increased antigenomic signal in the cytoplasm, suggesting an impaired localization (**Fig 4A**). While
401 images appear to suggest this, further quantification is necessary to conclude whether the increased
402 cytoplasmic signal compensates for the signal from the perinuclear region in these mutants.

403 Finally, we note that the smFISH probes we used would, in theory, also be complementary to
404 siRNAs. During antiviral RNAi, 1° siRNAs are generated from both strands of dsRNA during cleavage
405 by the DCR-1-DRH-1-RDE-4 complex, followed by association of RDE-1 with one strand of the siRNA.
406 Since we observed a perinuclear signal only with the antigenome probe (**Figs 3D and 3E**), if the
407 perinuclear signal resulted from hybridization to siRNAs, it seems most likely to arise from the single-
408 stranded siRNA that is delivered by RDE-1 to the viral genome for subsequent 2° siRNA amplification
409 by the host RdRP, RRF-1 [29,57]. However, we did not observe an effect on perinuclear antigenome
410 signal in animals lacking RDE-1 (**Fig 4),** nor a colocalization of RDE-1 with the perinuclear antigenome
411 puncta (**Fig 5G).** Further, while we cannot rule out the possibility that the perinuclear signal is due to
412 hybridization with an antisense siRNA, the 48 probes used to detect antigenome were uniformly
413 distributed along the length of the antigenome, and if it occurred, spurious complementarity to 2°

414 siRNAs would likely be to only part of the siRNA, and thus, unlikely to generate a robust signal. That
415 said, we cannot completely rule out this possibility.

416 **What is the nature of dsRNA induced during OV infection?**

417 During infection by both DNA and RNA viruses, dsRNA accumulates in infected cells, typically in
418 the cytoplasm [58]. The large majority of existing studies detect dsRNA using commercially available
419 antibodies [30,59], and the dsRNA is inferred to be of viral origin because it correlates with infection,
420 and in some cases is observed associated with the viral RdRP [60]. Indeed, using an antibody to
421 dsRNA, we and others have observed dsRNA accumulation in OV-infected intestinal cells (**Fig 6B;** [5]).
422 In our experiments, we were only able to detect antigenome upon denaturation (**Fig 2A**), suggesting
423 the antigenome is basepaired, either intramolecularly or in dsRNA formed between the genome and
424 antigenome. Previous observations of oRdRP show a cytoplasmic distribution in OV-infected cells [3],
425 and in our studies, in wildtype and *rde-1* mutant animals, we find cytoplasmic dsRNA puncta associated
426 with oRdRP, consistent with a viral origin (**Fig 6B**). These dsRNA-associated oRdRP puncta are
427 possible viral replication hubs, similar to previous observations in other +ssRNA virus infections [47,60].
428 We also observed closely associating genome and antigenome cytoplasmic puncta suggestive of
429 replication hubs (**Figs 3F and 3H**). Future studies will also focus on identifying colocalized antigenome
430 and oRdRP to confirm the presence of cytoplasmic replication hubs. dsRNA puncta that lack
431 association with oRdRP could be partially processed dsRNAs or siRNAs.

432 As in prior studies that used antibodies to detect dsRNA after viral infection of mammalian cells
433 [58], we also observed dsRNA in the nucleus. A robust nuclear J2 signal was observed only after viral
434 infection (**Fig 6B, *jyIs8*, dsRNA**), in *pals-5p::GFP* positive cells, but not in neighboring *pals-5p::GFP*
435 negative cells. While it is possible that this dsRNA is of viral origin, we favor the idea that it derives from
436 infection-induced transcription of endogenous genes that contain intronic dsRNA, which are prevalent
437 in many animals [31]. Among the differentially-expressed genes produced during OV infection [2,11],
438 some do contain introns that encode dsRNA, such as *zip-1* and *uggt-2*, as defined in Reich et.al. [25].
439 Interestingly the nuclear dsRNA signal is observed in wildtype-infected nuclei but not in *rde-1* animals
440 (**Fig 6B**), possibly due to their inefficient antiviral response. This also highlights the importance of

441 investigating antiviral responses in a wildtype background, since unique host responses to OV may not
442 always be evident in mutant strains.

443 **What are oRdRP spheres?**

444 Prior studies have only visualized oRdRP in RNAi mutant backgrounds at late larval stages,
445 possibly explaining why these spherical structures were missed previously [3]. While typical viral
446 replication organelles are ~300nm in diameter, we observed oRdRP-rimmed mitochondrially-associated
447 spheres (**Figs 7A, 7B**), that were larger, ~1μm in diameter (**Fig 6D**), and in contrast to replication
448 organelles, lacked association with dsRNA (**Fig 6B**). Further, even though *rde-1* mutant animals are
449 more permissive to virus, they exhibited reduced oRdRP spheres (**Figs 6B and 6C**), consistent with the
450 idea that spheres are not replication organelles. While higher resolution analyses are required to
451 determine the nature and function of oRdRP sphere interaction with cellular organelles, one intriguing
452 possibility is that these are structures associated with viral clearance.

453 Endoplasmic reticulum (ER) networks, specifically rough ER, are predominantly found in the
454 region surrounding the nucleus, often connected to the outer nuclear membrane. ER and ER quality
455 control (ERQC) mechanisms are hijacked by viruses to aid in their replication and assembly [61,62].
456 Notably, oRNA1 and capsid proteins also associate with ER during infection [63], suggesting ER as a
457 site for translation of viral proteins and its packaging. Consistent with this, at 24hpi, we observed a
458 distinct peak in genomic strand surrounding the nucleus (**Fig 3**). Given that oRdRP does not get
459 packaged, it must be cleared by the host. One possibility is that the oRdRP spheres we observe at
460 24hpi (**Fig 6B**) are formed from the remnants of replication sites targeted by the host for clearance. In
461 other viral infection models, viral RdRP is ubiquitinated and degraded through autophagy or
462 proteosome degradation pathways [43], and between 12hpi and 24hpi with OV, genes related to
463 ubiquitin-proteasome pathways are induced [2,11]. We observed that mutation of ATG-3, a protein
464 involved in the formation of autophagosomes, or RDE-1, a protein involved in ER-associated silencing
465 (ERAS), caused a reduction in the number of oRdRP spheres (**Figs 6C and 7C**), suggesting a link to
466 autophagy and RNAi/ERAS, respectively. In *C. elegans*, infection with OV also induced GFP::LGG-1
467 puncta, which showed partial association with ubiquitin puncta [19]. Given that some oRdRP spheres

468 themselves associate with autophagosomes (**Figs 7D and 7E**), it will be important in future studies to
469 determine whether or not the oRdRP in spheres is ubiquitinated by the host machinery and targeted for
470 degradation through autophagy post viral replication.

471 **Materials and Methods**

472 ***C. elegans* growth and maintenance**

473 All *C. elegans* strains were cultured at 20°C under standard conditions unless specified [64]. The list of
474 strains used in this study can be found in S1 Table. Some strains were provided by the CGC, which is
475 funded by NIH Office of Research Infrastructure Programs (P40 OD010440).

476 **Orsay virus filtrate preparation**

477 OV filtrate was prepared, and viral titer calculated, as described [16]. Briefly, JU1580 strain was
478 cultured in S medium [55] and infected with OV for 3 days. Following infection, supernatant was
479 collected and passed through a 0.22μm filter. The resulting filtrate was aliquoted and flash frozen at -
480 80°C for long term storage. To calculate viral titer, *rde-1(ne219)* animals (1000 L1 per plate) were
481 infected with serial dilutions (10-fold dilutions prepared in M9 buffer) of the viral filtrate.

482 **Orsay virus infection**

483 For viral load, strand-specific PCR (ss-qPCR), northern blot and dot blot experiments: Strains were
484 grown to gravid adults in liquid medium. Gravid adults were bleached (10% NaOH, 20% bleach), and
485 embryos were synchronized in M9 buffer overnight at 20°C. For L3 infection experiments, 2000
486 synchronized L1s were plated in OP50-containing NGM plates and grown for 39 hours at 20° and
487 infected with 0.1X OV for either 12 hours or 24 hours. For L1 infection experiments, 2000 synchronized
488 L1s were plated in OP50-containing NGM plates and infected with 0.1X OV for 48 or 72 hours. The
489 resulting infected and uninfected animals were washed in M9 buffer 4 times and collected in Trizol for
490 RNA extraction.

491 For intestinal dissection: ~200 synchronized L1 animals were transferred to a plate containing OP50.
492 Animals were incubated for 44-48 hours until they reached late larval stage (L3/L4). Animals were
493 infected with OV (0.1X or 1X) for 24 hours and collected for dissections.

494 For smFISH experiments: ~300-500 synchronized L1s of respective strains were plated on OP50-
495 containing plates and infected with OV (1X) at 20°C. Infected animals were collected after 24 hours of
496 infection.

497 **RNA extraction, cDNA synthesis and qPCR**

498 Total RNA from worms was collected using Trizol-chloroform-isopropanol extraction. Briefly, animals
499 frozen in Trizol were thawed, and chloroform was added. Aqueous layer was separated, and RNA was
500 precipitated using 100% isopropyl alcohol by incubating at room temperature for 30 minutes. The
501 resulting pellet was washed and treated with DNase. DNase-treated RNA was then purified using Zymo
502 RNA pure column as per manufacturer's instructions. The resulting total RNA was used for all
503 downstream analyses. cDNA was synthesized using Applied Biosystems cDNA synthesis kit as per
504 manufacturer's protocol for all experiments involving random hexamers. qPCR was performed using a
505 QuantStudio3 instrument. Primers for qPCR are listed in S2 Table. Ct values were normalized to levels
506 of *cdc-42*, and fold change was calculated using the ΔΔCt method [66].

507 **Strand-specific RT-qPCR**

508 We used strand-specific probes designed to bind the middle of one of the two Orsay RNA1 (oRNA1)
509 strands; each probe also included a unique adapter sequence that did not bind within the viral genome
510 or antigenome. To synthesize first strand cDNA, we incubated the probe with RNA and 10mM dNTP at
511 60°C for 10 mins, followed by reverse transcription at 37°C for 1 hour using the Applied Biosystems
512 cDNA synthesis kit; enzyme was inactivated at 85°C for 20 minutes. We then used this strand-specific
513 cDNA for qPCR. The unique adapter sequence was used as a forward primer combined with a reverse
514 primer complementary to a region on the same strand of oRNA1, for qPCR. Primers are listed in S3
515 Table.

516 **Dot blot assay**

517 Dot blot assays were performed as described [30] with slight modifications. Briefly, 500ng of total RNA
518 was diluted to 4μl and carefully spotted onto a supercharged nylon membrane. Once dried, the
519 membrane was crosslinked under UV light (UV Stratalinker 1800, auto-crosslink setting). The cross-
520 linked membrane was blocked in blocking buffer (1X PBS, 0.05% Tween-20, 50mg/ml sheared salmon
521 sperm DNA, 5% skim milk) for 1 hour at room temperature (RT). The membrane was incubated with
522 primary antibody (Anti-dsRNA:J2, 1:2000) overnight at 4°C. The membrane was then washed thrice
523 with 1X PBST (1X PBS, 0.05% Tween-20) for 10 minutes at RT. The membrane was then incubated
524 with secondary antibody (Anti-mouse IR dye 800CW, 1:20,000) for 1 hour at RT. The membrane was

525 washed twice with 1XPBST for 10 minutes at RT, followed by two washes with 1X PBS for 10 minutes
526 at RT. The membrane was then imaged using a LI-COR Odessey Infrared Imager. Antibodies were
527 diluted in antibody dilution buffer (1X PBS, 0.05% tween-20, 2% skim milk). In-vitro synthesized and
528 gel-purified ~800bp dsRNA was used as control for the dot blot assay.

529 **Intestine dissection, immunostaining**

530 Dissection and immunostaining protocols were based on [56] with modifications as below. Briefly, GFP+
531 infected animals were picked onto 20μl of 5μM levamisole. Worms were dissected using sterilized
532 surgical blades and transferred to 1X M9 buffer. Dissected intestines were washed twice with 1X M9,
533 twice with 1X PBST and fixed in 4% paraformaldehyde at RT for 15 minutes. Fixed intestines were
534 washed thrice with 1X PBST and blocked using a blocking solution (1X PBS, 0.5% Tween-20, 5%
535 Bovine Serum Albumin, 0.5% Sodium azide) at 4°C overnight. Following blocking, intestines were
536 incubated with Anti-oRdRP antibody (gift from Dr. David Wang [3]) and Anti-dsRNA (J2) antibody for 1-2
537 hours at RT. Unbound primary antibodies were washed off with 1X PBST, followed by incubation with
538 secondary antibodies for 1-2 hours at RT. This was followed by two washes with 1X PBST and one
539 wash with 1X PBST containing Hoechst (0.1ng/mL). For lipid droplet staining, LipidSpot™ 610 Lipid
540 droplet stain was diluted in 1X PBST and incubated for 30mins before Hoechst staining.
541 Immunostained intestines were stored in 1X PBST at 4°C until mounting and imaging. Antibodies were
542 diluted in blocking solution as per manufacturer's recommendations. Antibody information is listed in S3
543 Table.

544 **smFISH**

545 ~200 synchronized L1s of *jyIs8* or *jyIs8;rde-1* were plated on OP50-containing plates and infected with
546 OV at 20°C. Infected animals were collected after 24 hours of infection. Animals were washed with 1X
547 M9 buffer and 1X PBST (1X PBS, 0.05% Tween-20) and then fixed in 4% paraformaldehyde for 15
548 minutes at RT. Fixed animals were washed thrice with 1X PBST, followed by permeabilization in 70%
549 ethanol in 1X PBST for at least 2 hours at 4°C. Permeabilized worms were washed thrice with 1X PBST
550 to remove residual ethanol. If applicable, denaturation of dsRNA was performed by treating worms with
551 50mM sodium hydroxide for ~30 seconds at RT [21] and immediately washing twice with 1X PBST. This

552 was followed by a wash with 2X SSC buffer (Saline-Sodium Citrate), and then animals were pre-
553 hybridized in 1 mL of Wash Buffer A (Stellaris® RNA FISH Wash Buffer A with nuclease-free water and
554 10% formamide). Samples were then hybridized to probes for the genome (27 probes) and antigenome
555 (48 probes) (1μl of 12.5μM of each probe mix) in 100μl of hybridization buffer (Stellaris® RNA FISH
556 Hybridization buffer with freshly added 10% formamide) per sample. Samples were incubated at 37°C
557 overnight at 1200rpm (vortex). Post-hybridization, Wash Buffer A was directly added to samples
558 followed by incubation at 37°C for 30 minutes (vortex). Pellet was washed with Wash Buffer A with
559 Hoechst (0.1ng/mL) at 37'C or 30 minutes (vortex), followed by Stellaris® RNA FISH Wash Buffer B for
560 5 mins at RT on the nutator and then washed once with 1X PBST. Hybridized samples were stored in
561 1X PBST at 4°C until imaging. The sequences of the smFISH probes are listed in S4 Table.

562 **Imaging**

563 Animals were mounted onto 2% agarose pads using Vectashield mounting solution. Images were
564 captured using a DeltaVision Widefield Microscope with a 60X (oil) objective, Numerical Aperture
565 (NA=1.42), equipped with a sCMOS digital camera using the Blue-Green-Orange-Far Red channels or
566 Blue-Green-Red-Far Red channels. Multiple Z-slices spanning the entire thickness of the intestine with
567 Z-stacks 0.2μM apart were captured. Images were captured and deconvolved using the softWoRx
568 image processing software using standard settings. Individual channels were minimally adjusted in FIJI
569 for better visualization. Unless otherwise specified, a single Z-slice was used to represent data.
570 Acquisition setting for smFISH: Genome (Far-red), 5% transmission, 0.015-0.075 second exposure.
571 Antigenome (Orange), 30-50%transmission, 0.200-0.500 second exposure. Note that antigenome
572 channel was exposed for at least 10X longer than the genome channel.

573 **Quantification of perinuclear puncta distribution of oRNA1 antigenome**

574 Deconvolved and processed images were opened on ImageJ, and colors were assigned for genome
575 (cyan) and antigenome (magenta) channels. A composite image was created with a merge of these
576 channels. Animals with at least one perinuclear puncta enriched for antigenome and negative for
577 genome were considered a positive hit (visualized through line scan analysis). Randomization and blind
578 quantification were performed with the help of Bass lab members to account for user bias.

579 **Quantification of oRdRP spheres**

580 Deconvolved and processed images were used to perform oRdRP sphere diameter quantification on
581 minimally adjusted Z-slices for the oRdRP channel. Progressive z-slices showing a point progressing to
582 a circle and ending back in a point, was considered a sphere. Center z-slice of the sphere was
583 determined, and the diameter (from a single z-slice) was calculated using the line tool on ImageJ.
584 Randomization and blind quantification were performed with the help of Bass lab members to account
585 for user bias.

586 **Quantification of association of oRdRP with mitochondria and autophagosomes**

587 Deconvolved and processed images were used to perform line scan analyses on minimally adjusted Z-
588 slices of widefield images for oRdRP and wrmScarlet (mitochondria) or GFP (autophagosome)
589 channels.

590 **Heat shock inducible transgenic replicon system: heat shock induction protocol**

591 Transgenic array, GFP positive (in pharynx) animals (4-5 L4s) were picked onto a fresh OP50-
592 containing plate. Animals were incubated at 20°C for 3 days. Once they reached L4 larval stage,
593 animals were heat shocked at 34°C for 2 hours. Animals were collected after 24 hours of recovery at
594 20°C for strand-specific RT-qPCR and northern blot assays.

595 **Standard curve for strand-specific RT-qPCR**

596 In the region where the strand-specific primers were designed to bind oRNA1, a 500bp region was
597 amplified using primers flanking a T7 promoter (genome) or SP6 promoter (antigenome). The purified
598 PCR product was then used for in-vitro transcription to generate the genomic or antigenomic strand
599 using T7 or SP6 RNA polymerase, respectively. Known numbers of purified ssRNA strands, ranging
600 from 10^9 to 10^2 copies, were used for reverse transcription using strand-specific primers to generate
601 cDNA. The resulting cDNA was used for qPCR to generate a standard curve with copy number on the
602 x-axis and cycle threshold (Ct) values on the y-axis. Standard curve was generated, and the equation
603 was obtained by fitting points to a semi-log line using GraphPad Prism software. The resulting equation
604 was then used to determine copy number for strand-specific RT-qPCR analysis of infection
605 experiments.

606 **Northern blot**

607 Total RNA purified from early and late infected animals was heated at 65°C for 10 minutes in northern
608 loading buffer containing ethidium bromide. Buffers were prepared and northern blot was performed as
609 described in [57]. Membrane was then imaged under short UV light to capture ethidium bromide
610 staining for the loading control. Membrane was pre-hybridized using hybridization buffer at 42°C for 20-
611 30 minutes. 50μL purified, and end-labeled probes were mixed with hybridization buffer and added to
612 the membrane for hybridization overnight at 42°C; membranes were then washed with northern wash
613 buffer thrice. Antigenome hybridized membranes were exposed to a PhosphorImager screen for 3
614 days; genome hybridized membranes were exposed for 2-3 hours; 72hpi sample containing membrane
615 was only exposed for 15 minutes. PhosphorImage screens were imaged with a Typhoon Biomolecular
616 Imager.

617 **CRISPR-Cas9 for *rde-4(uu71)* generation**

618 *rde-4(uu71)* allele was generated with the CRISPR/Cas9 system as described [25].

619 **Acknowledgements**

620 We thank Bass lab members for helpful discussions and feedback. We thank Ryan Andrews for initial
621 help with imaging of smFISH experiments. We thank Adam Hughes, Minna Roh-Johnson, Nidhi
622 Raghuram, Ofer Rog and Sara Wong for helpful suggestions and feedback on microscopy data and
623 methods. We acknowledge the Cell Imaging Core at the University of Utah for use of equipment
624 (DeltaVision Ultra Widefield Microscope). Anti-RdRP (OV) antibody was a kind gift from Dr. David
625 Wang. We thank Dr. Will Mair for providing the WBM1689 strain. This work was supported by funding to
626 B.L.B. from the National Institute of General Medical Sciences (R35GM141262) and the National
627 Cancer Institute of the National Institutes of Health (R01CA260414). B.L.B. is a Jon M. Huntsman
628 Presidential Endowed Chair.

629 **References**

630 1. Félix M-A, Ashe A, Piffaretti J, Wu G, Nuez I, Bélicard T, et al. Natural and Experimental Infection of
631 Caenorhabditis Nematodes by Novel Viruses Related to Nodaviruses. PLOS Biol. 2011;9:
632 e1000586. doi:10.1371/journal.pbio.1000586

633 2. Castiglioni VG, Olmo-Uceda MJ, Villena-Giménez A, Muñoz-Sánchez JC, Legarda EG, Elena SF.
634 Story of an infection: Viral dynamics and host responses in the Caenorhabditis elegans-Orsay
635 virus pathosystem. Sci Adv. 2024;10: eadn5945. doi:10.1126/sciadv.adn5945

636 3. Franz CJ, Renshaw H, Frezal L, Jiang Y, Félix M-A, Wang D. Orsay, Santeuil and Le Blanc viruses
637 primarily infect intestinal cells in *Caenorhabditis* nematodes. Virology. 2014;448: 255–264.
638 doi:10.1016/j.virol.2013.09.024

639 4. Félix M-A, Wang D. Natural Viruses of Caenorhabditis Nematodes. Annu Rev Genet. 2019;53: 313–
640 326. doi:10.1146/annurev-genet-112618-043756

641 5. Batachari LE, Dai AY, Troemel ER. Caenorhabditis elegans RIG-I-like receptor DRH-1 signals via
642 CARDs to activate antiviral immunity in intestinal cells. Proc Natl Acad Sci. 2024;121:
643 e2402126121. doi:10.1073/pnas.2402126121

644 6. de Beijer NL, Snijder EJ, Bárcena M. A Cool Look at Positive-Strand RNA Virus Replication
645 Organelles: New Insights from Cryo-Electron Microscopy. Annu Rev Biochem. 2024;93: 163–187.
646 doi:10.1146/annurev-biochem-052521-115736

647 7. Stancheva VG, Sanyal S. Positive-strand RNA virus replication organelles at a glance. J Cell Sci.
648 2024;137: jcs262164. doi:10.1242/jcs.262164

649 8. Ball LA. Replication of the genomic RNA of a positive-strand RNA animal virus from negative-sense
650 transcripts. Proc Natl Acad Sci U S A. 1994;91: 12443–12447.

651 9. Guo X, Zhang R, Wang J, Ding S-W, Lu R. Homologous RIG-I–like helicase proteins direct RNAi-
652 mediated antiviral immunity in C. elegans by distinct mechanisms. Proc Natl Acad Sci U S A.
653 2013;110: 16085–16090. doi:10.1073/pnas.1307453110

654 10. Ashe A, Bélicard T, Le Pen J, Sarkies P, Frézal L, Lehrbach NJ, et al. A deletion polymorphism in
655 the Caenorhabditis elegans RIG-I homolog disables viral RNA dicing and antiviral immunity. eLife.
656 2013;2: e00994. doi:10.7554/eLife.00994

657 11. Chen K, Franz CJ, Jiang H, Jiang Y, Wang D. An evolutionarily conserved transcriptional response
658 to viral infection in Caenorhabditis nematodes. BMC Genomics. 2017;18. doi:10.1186/s12864-
659 017-3689-3

660 12. Reddy KC, Dror T, Sowa JN, Panek J, Chen K, Lim ES, et al. An Intracellular Pathogen Response
661 Pathway Promotes Proteostasis in C. elegans. Curr Biol CB. 2017;27: 3544-3553.e5.
662 doi:10.1016/j.cub.2017.10.009

663 13. Sowa JN, Jiang H, Somasundaram L, Tecle E, Xu G, Wang D, et al. The C. elegans RIG-I homolog
664 DRH-1 mediates the Intracellular Pathogen Response upon viral infection. J Virol. 2019 [cited 7
665 Nov 2019]. doi:10.1128/JVI.01173-19

666 14. Welker NC, Pavelec DM, Nix DA, Duchaine TF, Kennedy S, Bass BL. Dicer's helicase domain is
667 required for accumulation of some, but not all, C. elegans endogenous siRNAs. RNA. 2010;16:
668 893–903. doi:10.1261/rna.2122010

669 15. Pavelec DM, Lachowiec J, Duchaine TF, Smith HE, Kennedy S. Requirement for the ERI/DICER
670 complex in endogenous RNA interference and sperm development in Caenorhabditis elegans.
671 Genetics. 2009;183: 1283–1295. doi:10.1534/genetics.109.108134

672 16. Jiang H, Chen K, Sandoval LE, Leung C, Wang D. An Evolutionarily Conserved Pathway Essential
673 for Orsay Virus Infection of Caenorhabditis elegans. mBio. 2017;8. doi:10.1128/mBio.00940-17

674 17. Ahlquist P, Noueiry AO, Lee W-M, Kushner DB, Dye BT. Host Factors in Positive-Strand RNA Virus
675 Genome Replication. J Virol. 2003;77: 8181–8186. doi:10.1128/JVI.77.15.8181-8186.2003

676 18. Jakubiec A, Jupin I. Regulation of positive-strand RNA virus replication: The emerging role of
677 phosphorylation. Virus Res. 2007;129: 73–79. doi:10.1016/j.virusres.2007.07.012

678 19. Bakowski MA, Desjardins CA, Smelkinson MG, Dunbar TA, Lopez-Moyado IF, Rifkin SA, et al.
679 Ubiquitin-Mediated Response to Microsporidia and Virus Infection in C. elegans. PLOS Pathog.
680 2014;10: e1004200. doi:10.1371/journal.ppat.1004200

681 20. Lažetić V, Wu F, Cohen LB, Reddy KC, Chang Y-T, Gang SS, et al. The transcription factor ZIP-1
682 promotes resistance to intracellular infection in Caenorhabditis elegans. Nat Commun. 2022;13:
683 17. doi:10.1038/s41467-021-27621-w

684 21. Genoyer E, Wilson J, Ames JM, Stokes C, Moreno D, Etzyon N, et al. Exposure of negative-sense
685 viral RNA in the cytoplasm initiates innate immunity to West Nile virus. Mol Cell. 2025;85: 1147-
686 1161.e9. doi:10.1016/j.molcel.2025.01.015

687 22. Fernández de Castro I, Tenorio R, Risco C. Virus Factories. Encycl Virol. 2021; 495–500.
688 doi:10.1016/B978-0-12-814515-9.00001-1

689 23. Miller DJ, Schwartz MD, Ahlquist P. Flock House Virus RNA Replicates on Outer Mitochondrial
690 Membranes in Drosophila Cells. J Virol. 2001;75: 11664–11676. doi:10.1128/JVI.75.23.11664-
691 11676.2001

692 24. Consalvo CD, Aderounmu AM, Donelick HM, Aruscavage PJ, Eckert DM, Shen PS, et al. C.
693 elegans Dicer acts with the RIG-I-like helicase DRH-1 and RDE-4 to cleave dsRNA. eLife.
694 2024;13. doi:10.7554/eLife.93979.2

695 25. Reich DP, Tyc KM, Bass BL. C. elegans ADARs antagonize silencing of cellular dsRNAs by the
696 antiviral RNAi pathway. Genes Dev. 2018;32: 271–282. doi:10.1101/gad.310672.117

697 26. Coffman SR, Lu J, Guo X, Zhong J, Jiang H, Broitman-Maduro G, et al. Caenorhabditis elegans
698 RIG-I Homolog Mediates Antiviral RNA Interference Downstream of Dicer-Dependent Biogenesis
699 of Viral Small Interfering RNAs. mBio. 2017;8. doi:10.1128/mBio.00264-17

700 27. Uebel CJ, Anderson DC, Mandarino LM, Manage KI, Aynaszyan S, Phillips CM. Distinct regions of
701 the intrinsically disordered protein MUT-16 mediate assembly of a small RNA amplification
702 complex and promote phase separation of Mutator foci. PLOS Genet. 2018;14: e1007542.
703 doi:10.1371/journal.pgen.1007542

704 28. Phillips CM, Montgomery TA, Breen PC, Ruvkun G. MUT-16 promotes formation of perinuclear
705 Mutator foci required for RNA silencing in the C. elegans germline. Genes Dev. 2012;26: 1433–
706 1444. doi:10.1101/gad.193904.112

707 29. Lowe D, Shukla A, Kennedy S. Viral RNA pUGylation Promotes Antiviral Immunity in C. elegans.
708 bioRxiv; 2025. p. 2025.07.09.663919. doi:10.1101/2025.07.09.663919

709 30. de Faria IJS, Imler J-L, Marques JT. Protocol for the analysis of double-stranded RNAs in virus-
710 infected insect cells using anti-dsRNA antibodies. STAR Protoc. 2023;4: 102033.
711 doi:10.1016/j.xpro.2022.102033

712 31. Reich DP, Bass BL. Mapping the dsRNA World. Cold Spring Harb Perspect Biol. 2019;11: a035352.
713 doi:10.1101/cshperspect.a035352

714 32. Miller DJ, Ahlquist P. Flock House Virus RNA Polymerase Is a Transmembrane Protein with Amino-
715 Terminal Sequences Sufficient for Mitochondrial Localization and Membrane Insertion. J Virol.
716 2002;76: 9856–9867. doi:10.1128/JVI.76.19.9856-9867.2002

717 33. Hallgren J, Tsirigos K, Pedersen MD, Almagro Armenteros JJ, Marcatili P, Nielsen H, et al.
718 DeepTMHMM predicts alpha and beta transmembrane proteins using deep neural network. 2022.
719 doi:10.1101/2022.04.08.487609

720 34. Tusnády GE, Simon I. The HMMTOP transmembrane topology prediction server. Bioinforma Oxf
721 Engl. 2001;17: 849–850. doi:10.1093/bioinformatics/17.9.849

722 35. Cserzö M, Wallin E, Simon I, von Heijne G, Elofsson A. Prediction of transmembrane alpha-helices
723 in prokaryotic membrane proteins: the dense alignment surface method. Protein Eng. 1997;10:
724 673–676. doi:10.1093/protein/10.6.673

725 36. Sonnhammer EL, von Heijne G, Krogh A. A hidden Markov model for predicting transmembrane
726 helices in protein sequences. Proc Int Conf Intell Syst Mol Biol. 1998;6: 175–182.

727 37. Krogh A, Larsson B, von Heijne G, Sonnhammer ELL. Predicting transmembrane protein topology
728 with a hidden markov model: application to complete genomes1. J Mol Biol. 2001;305: 567–580.
729 doi:10.1006/jmbi.2000.4315

730 38. Mak HY. Lipid droplets as fat storage organelles in Caenorhabditis elegans. J Lipid Res. 2012;53:
731 28–33. doi:10.1194/jlr.R021006

732 39. Shi X, Li J, Zou X, Greggain J, Rødkær SV, Færgeman NJ, et al. Regulation of lipid droplet size
733 and phospholipid composition by stearoyl-CoA desaturase. J Lipid Res. 2013;54: 2504–2514.
734 doi:10.1194/jlr.M039669

735 40. Casorla-Perez LA, Guennoun R, Cubillas C, Peng B, Kornfeld K, Wang D. Orsay Virus Infection of
736 Caenorhabditis elegans Is Modulated by Zinc and Dependent on Lipids. J Virol. 2022;96: e01211-
737 22. doi:10.1128/jvi.01211-22

738 41. Valera-Alberni M, Yao P, Romero-Sanz S, Lanjuin A, Mair WB. Novel Imaging Tools to Study
739 Mitochondrial Dynamics in Caenorhabditis elegans. bioRxiv; 2024. p. 2024.07.16.603730.
740 doi:10.1101/2024.07.16.603730

741 42. Choi Y, Bowman JW, Jung JU. Autophagy during viral infection — a double-edged sword. Nat Rev
742 Microbiol. 2018;16: 341–354. doi:10.1038/s41579-018-0003-6

743 43. Liang S, Wu Y-S, Li D-Y, Tang J-X, Liu H-F. Autophagy in Viral Infection and Pathogenesis. Front
744 Cell Dev Biol. 2021;9. doi:10.3389/fcell.2021.766142

745 44. Dawson ZD, Sundaramoorthi ,Hemalatha, Regmi ,Suk, Zhang ,Bo, Morrison ,Stephanie, Fielder
746 ,Sara M., et al. A fluorescent reporter for rapid assessment of autophagic flux reveals unique
747 autophagy signatures during C. elegans post-embryonic development and identifies compounds

748 that modulate autophagy. Autophagy Rep. 2024;3: 2371736.
749 doi:10.1080/27694127.2024.2371736

750 45. Fujita N, Itoh T, Omori H, Fukuda M, Noda T, Yoshimori T. The Atg16L complex specifies the site of
751 LC3 lipidation for membrane biogenesis in autophagy. Mol Biol Cell. 2008;19: 2092–2100.
752 doi:10.1091/mbc.e07-12-1257

753 46. Kalugotla G, Marmerstein V, Schriefer LA, Wang L, Morrison S, Perez LC, et al. ATG-3 limits Orsay
754 virus infection in C. elegans through regulation of collagen pathways. bioRxiv. 2025;
755 2025.01.13.632696. doi:10.1101/2025.01.13.632696

756 47. Shulla A, Randall G. Spatiotemporal analysis of hepatitis C virus infection. PLoS Pathog. 2015;11:
757 e1004758. doi:10.1371/journal.ppat.1004758

758 48. Novak JE, Kirkegaard K. Improved method for detecting poliovirus negative strands used to
759 demonstrate specificity of positive-strand encapsidation and the ratio of positive to negative
760 strands in infected cells. J Virol. 1991;65: 3384–3387. doi:10.1128/JVI.65.6.3384-3387.1991

761 49. Warncke SR, Knudsen CR. Detection methods targeting the positive- and negative-sense RNA
762 transcripts from plus-stranded RNA viruses. APMIS Acta Pathol Microbiol Immunol Scand.
763 2022;130: 284–292. doi:10.1111/apm.13202

764 50. Ivashkiv LB, Donlin LT. Regulation of type I interferon responses. Nat Rev Immunol. 2014;14: 36–
765 49. doi:10.1038/nri3581

766 51. Schreiber G. The molecular basis for differential type I interferon signaling. J Biol Chem. 2017;292:
767 7285–7294. doi:10.1074/jbc.R116.774562

768 52. Tanguy M, Véron L, Stempor P, Ahringer J, Sarkies P, Miska EA. An Alternative STAT Signaling
769 Pathway Acts in Viral Immunity in Caenorhabditis elegans. mBio. 2017;8.
770 doi:10.1128/mBio.00924-17

771 53. den Boon JA, Nishikiori M, Zhan H, Ahlquist P. Positive-strand RNA virus genome replication
772 organelles: structure, assembly, control. Trends Genet TIG. 2024;40: 681–693.
773 doi:10.1016/j.tig.2024.04.003

774 54. Huang X, Feng X, Yan Y, Xu D, Wang K, Zhu C, et al. Compartmentalized localization of perinuclear
775 proteins within germ granules in C. elegans. bioRxiv; 2024. p. 2024.03.25.586584.
776 doi:10.1101/2024.03.25.586584

777 55. Tsai H-Y, Chen C-CG, Conte D, Moresco JJ, Chaves DA, Mitani S, et al. A ribonuclease coordinates
778 siRNA amplification and mRNA cleavage during RNAi. Cell. 2015;160: 407–419.
779 doi:10.1016/j.cell.2015.01.010

780 56. Seroussi U, Lugowski A, Wadi L, Lao RX, Willis AR, Zhao W, et al. A comprehensive survey of C.
781 elegans argonaute proteins reveals organism-wide gene regulatory networks and functions.
782 James DE, Pasquenelli A, Kennedy S, editors. eLife. 2023;12: e83853. doi:10.7554/eLife.83853

783 57. Tabara H, Sarkissian M, Kelly WG, Fleenor J, Grishok A, Timmons L, et al. The rde-1 Gene, RNA
784 Interference, and Transposon Silencing in C. elegans. Cell. 1999;99: 123–132.
785 doi:10.1016/S0092-8674(00)81644-X

786 58. Son K-N, Liang Z, Lipton HL. Double-Stranded RNA Is Detected by Immunofluorescence Analysis
787 in RNA and DNA Virus Infections, Including Those by Negative-Stranded RNA Viruses. J Virol.
788 2015;89: 9383–9392. doi:10.1128/jvi.01299-15

789 59. Corbet GA, Burke JM, Bublitz GR, Tay JW, Parker R. dsRNA-induced condensation of antiviral
790 proteins modulates PKR activity. Proc Natl Acad Sci. 2022;119: e2204235119.
791 doi:10.1073/pnas.2204235119

792 60. Andronov L, Han M, Zhu Y, Balaji A, Roy AR, Barentine AES, et al. Nanoscale cellular organization
793 of viral RNA and proteins in SARS-CoV-2 replication organelles. Nat Commun. 2024;15: 4644.
794 doi:10.1038/s41467-024-48991-x

795 61. Romero-Brey I, Bartenschlager R. Endoplasmic Reticulum: The Favorite Intracellular Niche for Viral
796 Replication and Assembly. Viruses. 2016;8: 160. doi:10.3390/v8060160

797 62. Byun H, Gou Y, Zook A, Lozano MM, Dudley JP. ERAD and how viruses exploit it. Front Microbiol.
798 2014;5: 330. doi:10.3389/fmicb.2014.00330

799 63. Efstathiou S, Ottens F, Schütter L-S, Ravanelli S, Charmpilas N, Gutschmidt A, et al. ER-associated
800 RNA silencing promotes ER quality control. Nat Cell Biol. 2022;24: 1714–1725.
801 doi:10.1038/s41556-022-01025-4

802 64. Brenner S. The Genetics of CAENORHABDITIS ELEGANS. Genetics. 1974;77: 71–94.
803 doi:10.1093/genetics/77.1.71

804 65. Maintenance of C. elegans. doi:10.1895/wormbook.1.101.1

805 66. Livak KJ, Schmittgen TD. Analysis of relative gene expression data using real-time quantitative
806 PCR and the 2(-Delta Delta C(T)) Method. Methods San Diego Calif. 2001;25: 402–408.
807 doi:10.1006/meth.2001.1262

808 67. Batachari LE, Sarmiento MB, Wernet N, Troemel ER. Orsay Virus Infection in Caenorhabditis
809 elegans. Curr Protoc. 2024;4: e1098. doi:10.1002/cpz1.1098

810 68. He SL. Northern blot. Methods Enzymol. 2013;530: 75–87. doi:10.1016/B978-0-12-420037-
811 1.00003-8

812 69. Guo YR, Hryc CF, Jakana J, Jiang H, Wang D, Chiu W, et al. Crystal structure of a nematode-
813 infecting virus. Proc Natl Acad Sci. 2014;111: 12781–12786. doi:10.1073/pnas.1407122111

814 70. Pavelec DM, Lachowiec J, Duchaine TF, Smith HE, Kennedy S. Requirement for the ERI/DICER
815 Complex in Endogenous RNA Interference and Sperm Development in Caenorhabditis elegans.
816 Genetics. 2009;183: 1283–1295. doi:10.1534/genetics.109.108134

817

818 **Fig 1: Dynamics of oRNA1 strand-specific accumulation upon OV infection.**

819 (A) Schematic of strand-specific RT-qPCR of OV RNA1. Primers with unique adapters (green colors)
820 were used for reverse transcription to generate cDNA specifically from oRNA1 strands. Resulting cDNA
821 was used for qPCR with primers that recognize the unique adapter and a downstream region (in black,
822 half arrows). Schematics of (B) late larval (L3) and (C) early larval (L1) OV infection protocols. Number
823 of copies (per ng of total RNA) of oRNA1 genome and antigenome at (D) L3 or (E) L1 infection of
824 indicated strains and times. Data, mean with standard deviation (N=3, biological replicates). Black
825 asterisks, significance between indicated infection time point and previous time point for oRNA1
826 genomic strand; Two-way ANOVA, Uncorrected Fischer's LSD test. Pink asterisks, significance
827 between genome and antigenome at indicated timepoint as shown for N2; Ratio paired t-test. No
828 asterisks, no significant difference (See also S1 Fig). Number of copies of oRNA1 genome or
829 antigenome as measured by strand-specific RT-qPCR in (F) constitutively OV-infected JU1580 animals
830 (Dotted lines, copy number of genome or antigenome in N2 animals at 12hpi. Ratio paired t-test), and
831 (G) in strains expressing oRNA1^{WT} or oRNA1^{mut} with or without heat shock. Data are mean with
832 standard deviation (N=4, biological replicates). Ratio paired t-test. **, p-value<0.05; **, p-value<0.01; ***,*
833 *p-value<0.001; ****, p-value<0.0001*.

834 **Fig 2: oRNA1 antigenome is only detectible upon RNA denaturation**

835 (A) Representative smFISH images of uninfected (denatured) and infected animals (*jyIs8;rde-1*) with or
836 without dsRNA denaturation. *pals-5p::GFP* (green), oRNA1 genome (cyan), oRNA1 antigenome
837 (magenta), scale bar, 25μm. Column 4 shows an enlarged image of region boxed in column 3. White
838 arrowhead points to antigenome puncta. Pharynx signal (*) is from *mCherry*, a co-expression marker of
839 the integrated transgene (*jyIs8*). (N>3, biological replicates). Solid white lines outline animals, dashed
840 white lines outline infected intestinal cells. (B) Distribution of percent animals exhibiting antigenomic
841 signal (puncta) with or without denaturation (N=3, biological replicates). Total number of infected
842 animals is indicated. Representative images of OV-infected animals with or without denaturation using
843 either (C) antigenome or (D) genome smFISH probes only. oRNA1 genome (cyan), oRNA1 antigenome

844 (magenta), scale bar, 25μm. Solid white lines outline an animal, dashed white lines outline infected
845 intestinal cells, and white arrowhead points to antigenome puncta in column 3 (antigenome zoom of C).

846 **Fig 3: oRNA1 antigenome localizes to perinuclear foci**

847 (A) Representative images of *jyIs8(wt)* or *jyIs8;rde-1(ne219)* animals infected with OV for 24 hours
848 along with corresponding line scan analysis (yellow arrow shows path of scan). Columns 1-3 depict
849 *pals-5p::GFP* (green), oRNA1 genome (cyan), antigenome (magenta), respectively. Merge zoom
850 (column 4) shows an enlarged image of the region boxed in columns 2 and 3 with signal from genome
851 and antigenome. Scale bar, 25μm. Infected cells are outlined with a white solid line and nuclei
852 (Hoechst) with a white dotted line. Pharynx signal (*) is from *mCherry,* a co-expression marker of the
853 integrated transgene (*jyIs8*). (B) Violin plot showing number of nuclei surrounded by genome smFISH
854 signal in indicated strains. Unpaired t-test with Welch's correction, ***; *p=0.0003* (C) Bar graph showing
855 percentage of infected animals exhibiting perinuclear localization of oRNA1 antigenome in infected cells
856 of *jyIs8(wt)* or *jyIs8;rde-1(ne219).* N=4, biological replicates. Total number of infected animals is
857 indicated in gray above each bar. (D-J) Representative images and line scans (yellow arrow shows
858 path of scan) of *jyIs8 (wt)*-infected cells (white solid line) showing distribution pattern of oRNA1
859 antigenome (magenta) in (D, E) perinuclear, (F, G) cytoplasmic, or (H, I) cytoplasmic foci, in genome-
860 containing infected cells, or (J) lumen (cyan, white solid line outlines infected animal). Dotted lines
861 indicate nuclei in G+AG (column 4) to enable visualization of nuclei in other columns. In (H), showing
862 cytoplasmic antigenome puncta, nucleus is unmarked since it is on a different z-plane.

863 **Fig 4: Perinuclear localization of oRNA1 antigenome is partially dependent on primary siRNA**
864 **biogenesis but not secondary siRNA amplification**

865 (A) Representative images of OV-infected cells with distribution patterns of genome (G, cyan),
866 antigenome (AG, magenta) and nuclei (Hoechst, blue) at 24hpi. In column 1, infected worm is outlined
867 (solid white line) with total number (n) of infected animals visualized in all replicates. Scale bar, 25μm.
868 Columns 2, 3 & 4 show enlarged images of region boxed in column 1. Dotted lines indicate nuclei in
869 G+AG (column 4) to enable visualization of nuclei in other columns. (B) Violin plot showing number of
870 nuclei surrounded by genome smFISH signal in indicated strains. Kruskal-Wallis Multiple comparison

871 test, ***;p<0.01, ***; p<0.001, ****;p<0.0001.* (C) Quantification of percent infected animals exhibiting
872 perinuclear localization of oRNA1 antigenome at 24hpi in indicated strains. Data are mean with
873 standard deviation, N≥3, biological replicates. One-way ANOVA with Tukey's multiple comparison test.
874 **;p<0.05, ***;p<0.001.*

875 **Fig 5: Perinuclear localized oRNA1 antigenome does not colocalize with known antiviral RNAi**
876 **factors**

877 (A) Schematic of antiviral RNAi pathway. Maximum Intensity Projection images as labeled for DCR-
878 1::3XFLAG::GFP, GFP::3XFLAG::RDE-1, DRH-3::GFP::3XFLAG, genome (cyan), antigenome
879 (magenta) and merge in intestinal cells. Shown are localization patterns for uninfected animals (B, C,
880 D) or at 24hpi (E, G, H). Boxed region in (D) shows an enlarged image of perinuclear localized DRH-3
881 in germline (inset). Columns 2,3 & 4 in E, G and H show infected cell (white solid line) in region boxed
882 in column 1. White arrowheads point to GFP puncta. Number in column 3 (n) indicate the fraction of
883 infected animals with GFP puncta in infected cells. (F) Line scan analysis of DCR-1::3XFLAG::GFP
884 infected cell showing distribution pattern of genome, antigenome and DCR-1::3XFLAG::GFP. Yellow
885 arrow shows path of scan. Over 40 infected animals were scored among 2 independent replicates for
886 each strain. Scale bar, 25μm.

887 **Fig 6: oRdRP is present in spherical structures or dsRNA-associated puncta in OV infected cells**

888 (A) Representative dot blot spotted with total RNA from uninfected and OV infected animals at 72hpi;
889 probed with J2 anti-dsRNA (J2) antibody. (N=3, biological replicates). (B) Representative images of
890 uninfected or infected (24hpi) *jyIs8* (wt) or *jyIs8;rde-1* dissected intestines (white solid outline). Infection
891 was signaled by expression of *pals-5p::GFP* (green) and also visualized were oRdRP (gray), dsRNA
892 (red), merge (oRdRP and dsRNA). Nuclei (as marked by Hoechst) outlined with white dotted line. Red
893 arrowheads, possible co-localization of oRdRP and dsRNA; white arrowheads, oRdRP spherical
894 structures; yellow arrowhead, oRdRP sphere near dsRNA puncta. Scale bar, 25μm; merge zoom,10μm.
895 N≥4 biological replicates with at least 5 animals per replicate for *jyIs8*; N=3 biological replicates with at
896 least 5 animals per replicate for *jyIs8;rde-1*. (C) Quantification of number of oRdRP spheres per
897 infected animal in indicated strains. Unpaired t-test with Welch's correction*; *, p=0.0424*. (D) Distribution

898 of diameter of each sphere measured from the infected animals. Unpaired t-test with Welch's
899 correction*; *, p=0.0154*.

900 **Fig 7: oRdRP spheres associate with mitochondria and autophagosomes during OV infection.**
901 (A) Representative image of infected dissected intestines (solid white outline) showing oRdRP
902 distribution (gray) along with *wrmScarlet::timm-50* signal (red) and merge panels. Scale bar, 25μm. The
903 second row (inset) is zoomed-in image of the outlined region in OV infected panel. White arrowheads
904 point to oRdRP sphere associating with *wrmScarlet::timm-50*. N=3. (B) Line scan analysis showing
905 distribution patterns of oRdRP and *wrmScarlet::timm-50* as indicated. Yellow arrow shows path of scan.
906 (C) Quantification of number of oRdRP spheres per infected animal in indicated strains. Unpaired t-test
907 with Welch's correction. **, p=0.0379.* N=3 biological replicates. (D) Representative images of infected
908 intestine (solid white outline) of wildtype animal showing oRdRP distribution (gray) along with
909 autophagosome marker (green) and merge panels. Scale bar, 25μm. (E) Line scans showing
910 association of oRdRP (gray) and autophagosomes (green) as indicated in the boxed region from (D).
911 Yellow arrow shows path of scan.

912 **Fig 8: Viral replication intermediates observed in infected intestinal cells.**
913 Cartoon shown observed replication intermediates in context of a viral infection. Among the various
914 intermediates generated during viral replication, we highlight three intermediates that do not get
915 packaged into virions. (1) oRdRP, which we observed associated with dsRNA or in spherical structures
916 associated with mitochondria and/or autophagosomes, in an RDE-1- and ATG-3-dependent manner. (2)
917 Antigenome, generated as a template for replication, which we observed associated with genome in the
918 cytoplasm or present as distinct perinuclear puncta, devoid of genome, and dependent on the
919 generation of primary siRNAs but independent of secondary siRNA amplification. (3) dsRNA, which
920 gets processed by the antiviral RNAi complex to elicit antiviral RNAi response, which we observed as
921 puncta associating with oRdRP. OV capsid structure was adapted from PDB: 4NWV [69]. The antiviral
922 RNAi complex is to scale and was adapted from Consalvo et. al. [24].

923 **Supporting information**

924 **S1 Fig: Increase in viral load corresponds to increase in genomic strand in wildtype and RNAi**
925 **mutants.**

926 Strand-specific RT-qPCR of purified Genomic (A) or Antigenomic (B) strands of oRNA1 were used to
927 generate standard curves. Equations written in plot were used to determine copy number from strand-
928 specific RT-qPCR shown in Figs 1 and S1. (C) Representative PhosphorImage of dot blot spotted with
929 serial dilutions (10^8 to 10^2 copies) of an ~500nt fragment of purified genome or antigenome RNA and
930 probed using DNA oligonucleotides (end-labeled with ^{32}P γ-ATP) complementary to oRNA1 strands.
931 Fold change (Genome/Antigenome) of wildtype and RNAi mutants of L3 infected (D) or L1 infected (E)
932 animals at 12 or 24 hpi, as measured by strand-specific RT-qPCR. Data, mean with standard deviation.
933 Representative northern blots of L3 (F) or L1 (G) animals for indicated times of infection points along
934 with controls (JU1580, WUM32, WUM33) probed with DNA oligonucleotides (end-labeled with ^{32}P γ-
935 ATP) specific to oRNA1 genome or antigenome. Ribosomal RNA (rRNA) as loading control was
936 visualized with ethidium bromide after transfer to nylon membrane. Strand-agnostic Orsay viral load in
937 L3 (H) or L1 (I) animals after 12 or 24 hpi. Data, mean with standard deviation. One-way ANOVA with
938 Tukey's multiple comparison test; **, p-value<0.05; **, p-value<0.01*, N=3 . Related to Fig 1.

939 **S2 Fig: Establishing background signal in uninfected animals using genome or antigenome**
940 **smFISH probes.**

941 Representative images of uninfected animals indicating minimal to no background signal of smFISH
942 probes for oRNA1 genome (cyan), antigenome (magenta) and merge (genome and antigenome). Scale
943 bar, 25μm. Related to Fig 4.

944 **S3 Fig: J2 anti-dsRNA antibody can detect as low as 50pg of purified dsRNA**

945 Representative image of dot blot spotted with serial dilutions (50 ng to 5 pg) of in vitro synthesized and
946 purified 800-bp dsRNA, probed with J2 anti-dsRNA antibody (N>3). Related to Fig 6.

947 **S4 Fig: oRdRP open-reading frame showing predicted transmembrane domains and RdRP**
948 **motifs**

949 Schematic at bottom shows amino acid numbers from N to C terminus with regions of predicted
950 transmembrane domains (7-30 and 51-74) and conserved viral RdRP motifs (422-612) in black.
951 Hydrophobicity plot above used a window size of 17 amino acids and was calculated using the Kyte
952 and Doolittle method. Regions with hydrophobicity of >1.5 are shown in brackets.

953 **S5 Fig: oRdRP spheres do not contain lipids**

954 Representative images of uninfected and OV-infected (24hpi) intestines showing oRdRP (gray, anti-
955 oRdRP), lipid droplets (red, LipidSpot™ 610 Lipid Droplet Stain), merge and inset (region boxed in
956 merge column). White arrowheads point to lipid droplets (inset). N=3, biological replicates; Scale bar,
957 10μm.

958 **S1 Table:** List of *C. elegans* strains used in this study.

959 **S2 Table:** List of primers used in this study.

960 **S3 Table:** List of antibodies used in this study.

961 **S4 Table:** List of smFISH probes used in this study.

962 **Fig 1**

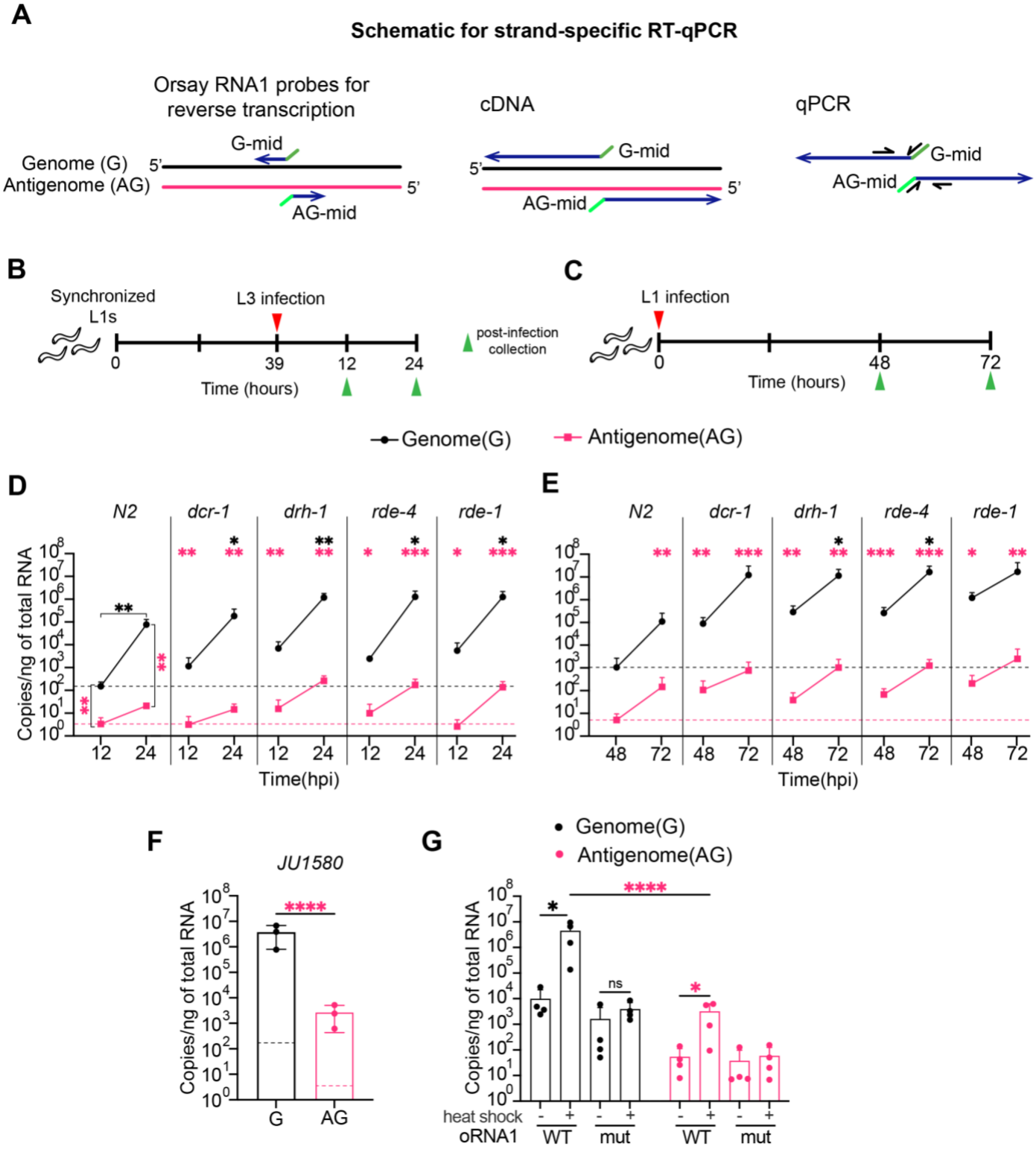
A
Schematic for strand-specific RT-qPCR
Orsay RNA1 probes for reverse transcription
cDNA
qPCR
Genome (G)
Antigenome (AG)
G-mid
AG-mid
5'
B
Synchronized L1s
L3 infection
post-infection collection
Time (hours)
C
L1 infection
Genome(G)
Antigenome(AG)
D
E
N2
dcr-1
drh-1
rde-4
rde-1
Copies/ng of total RNA
Time(hpi)
F
JU1580
G
heat shock
oRNA1
WT
mut
ns

963

964 **Fig 2**

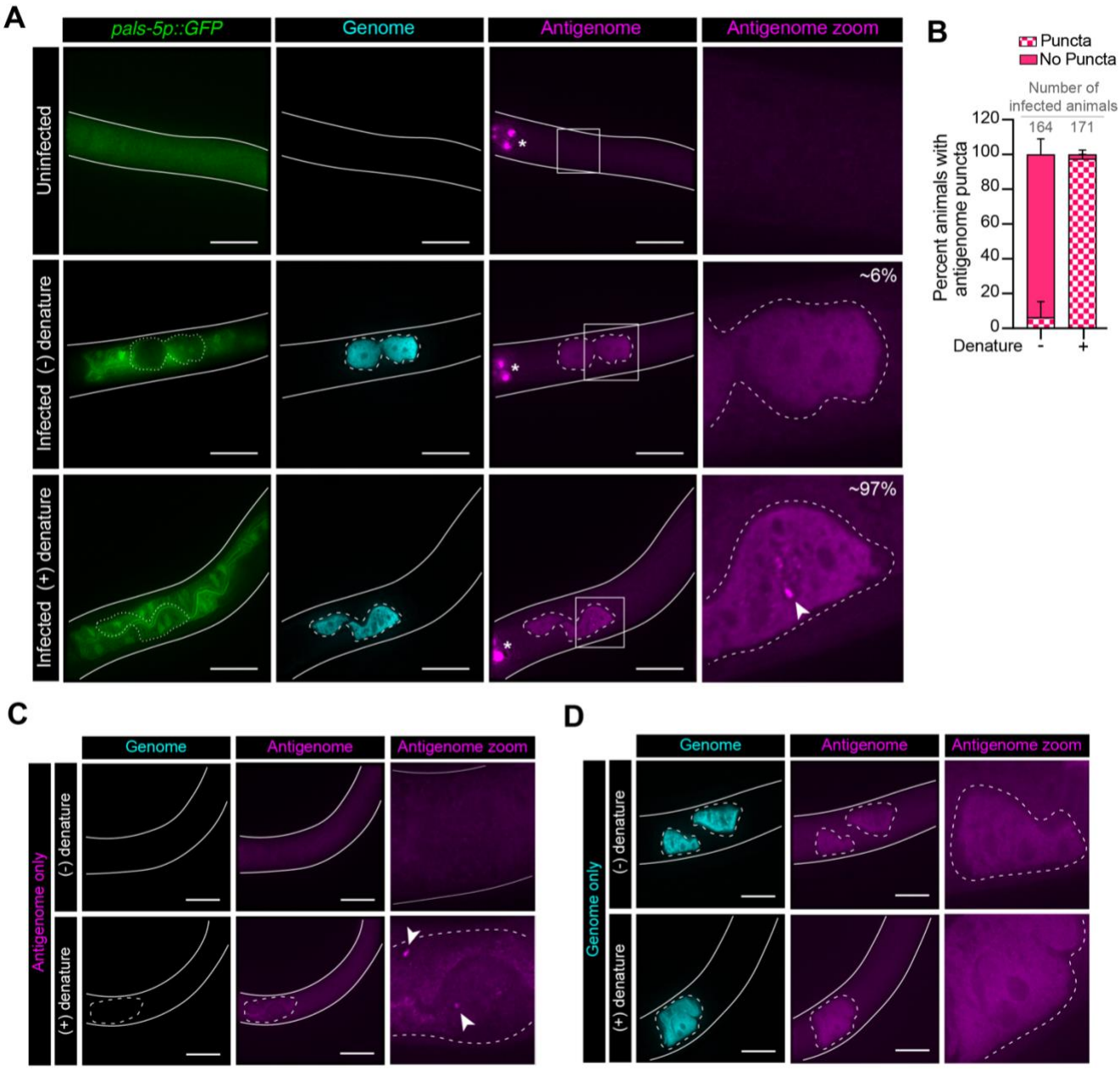
A
pals-5p::GFP
Genome
Antigenome
Antigenome zoom
Uninfected
Infected (-) denature
Infected (+) denature
~6%
~97%
B
Puncta
No Puncta
Number of infected animals
164
171
Percent animals with antigenome puncta
120
100
80
60
40
20
0
Denature
-
+
C
Genome
Antigenome
Antigenome zoom
Antigenome only
(-) denature
(+) denature
D
Genome
Antigenome
Antigenome zoom
Genome only
(-) denature
(+) denature

965

966 **Fig 3**

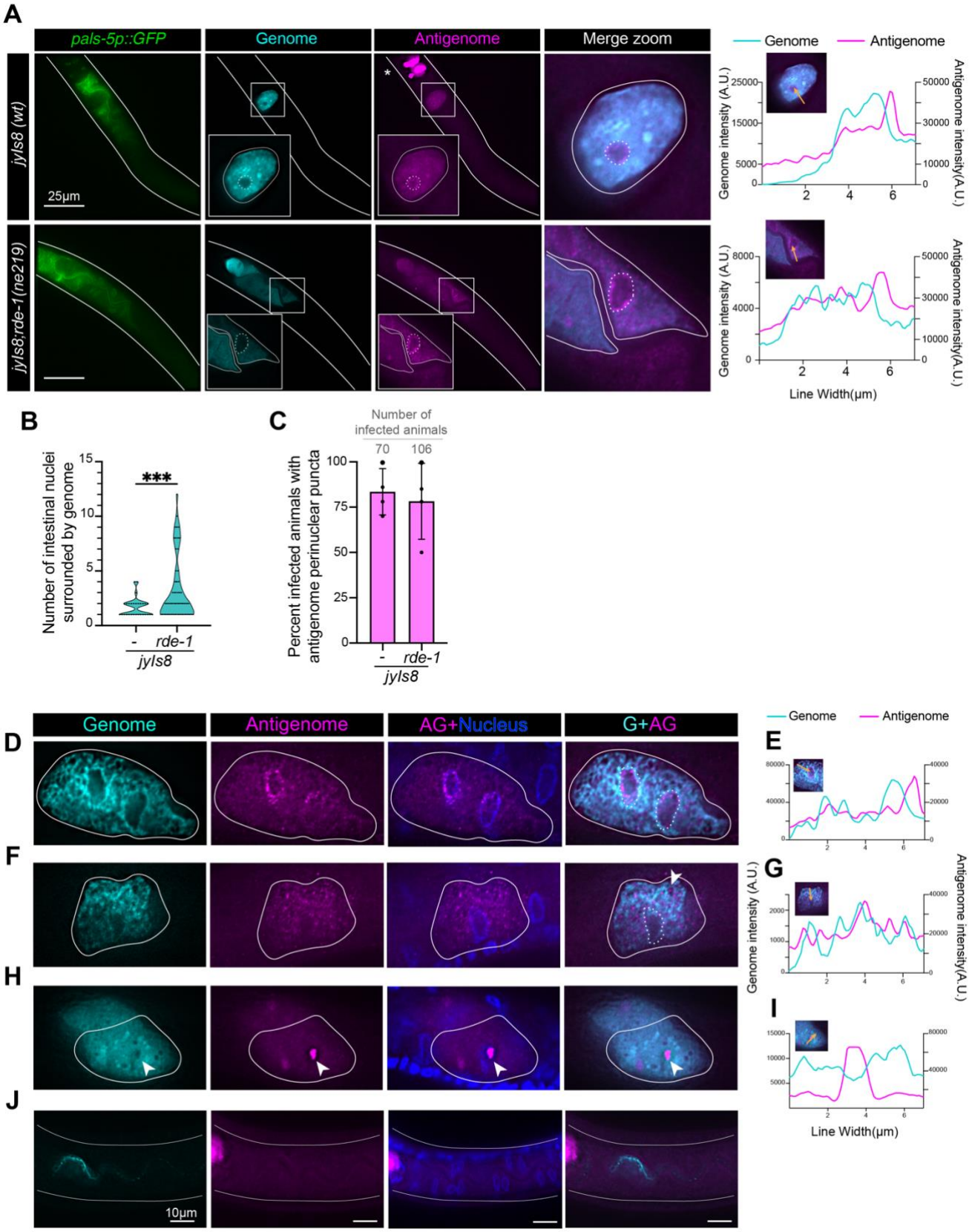
A
pals-5p::GFP
Genome
Antigenome
Merge zoom
jyIs8 (wt)
jyIs8;rde-1(ne219)
25µm
Genome
Antigenome
Genome intensity (A.U.)
Antigenome intensity(A.U.)
Line Width(µm)
B
Number of intestinal nuclei surrounded by genome
***
-
rde-1
jyIs8
C
Number of infected animals
70
106
Percent infected animals with antigenome perinuclear puncta
-
rde-1
jyIs8
D
F
H
J
Genome
Antigenome
AG+Nucleus
G+AG
E
G
I
Genome intensity (A.U.)
Antigenome intensity(A.U.)
Line Width(µm)
10µm

967

968 **Fig 4**

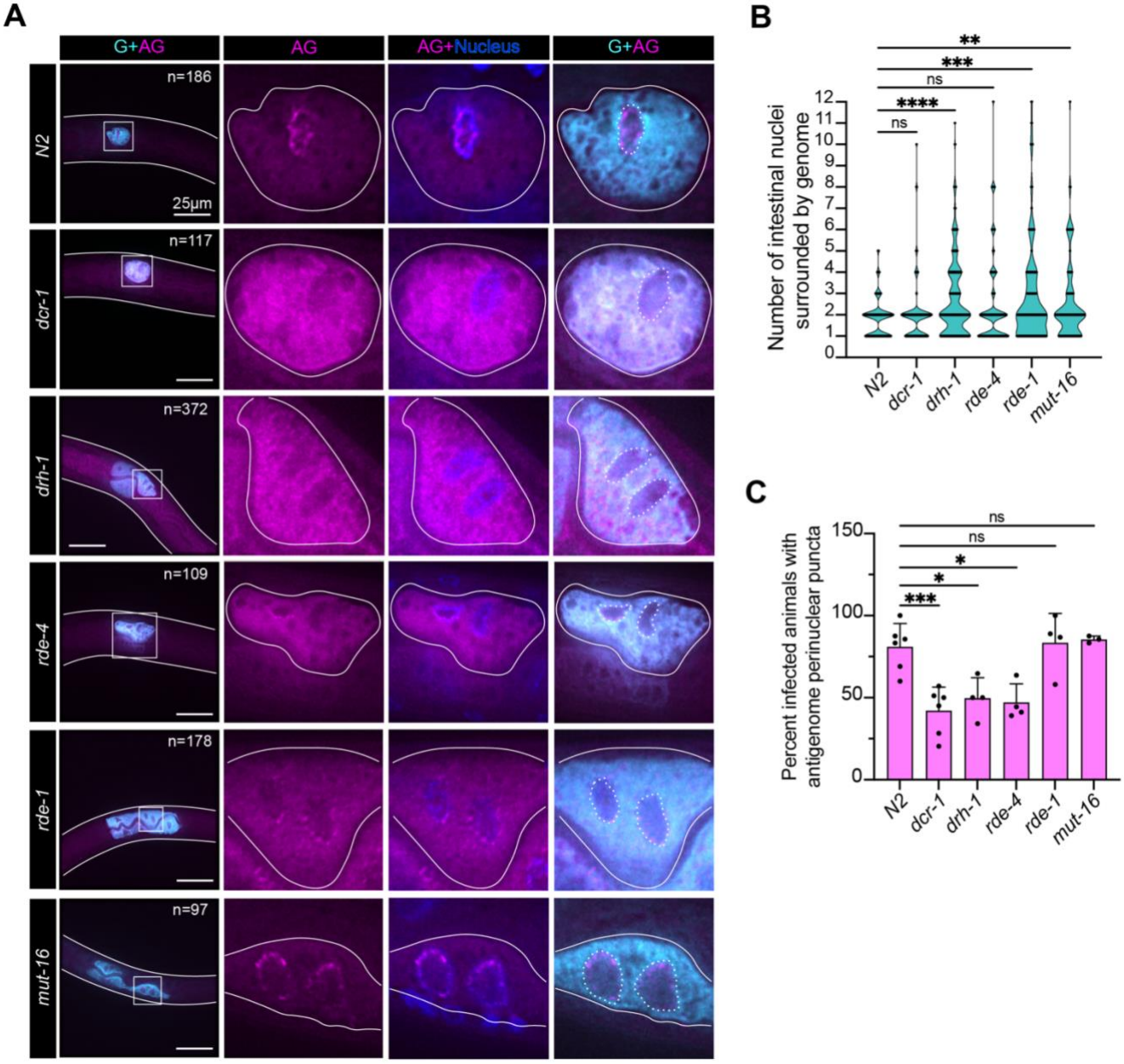
A
G+AG
AG
AG+Nucleus
G+AG
N2
n=186
25µm
dcr-1
n=117
drh-1
n=372
rde-4
n=109
rde-1
n=178
mut-16
n=97
B
Number of intestinal nuclei surrounded by genome
**
***
ns
****
ns
N2
dcr-1
drh-1
rde-4
rde-1
mut-16
C
Percent infected animals with antigenome perinuclear puncta
ns
ns
*
*
***
N2
dcr-1
drh-1
rde-4
rde-1
mut-16

969

970 **Fig 5**

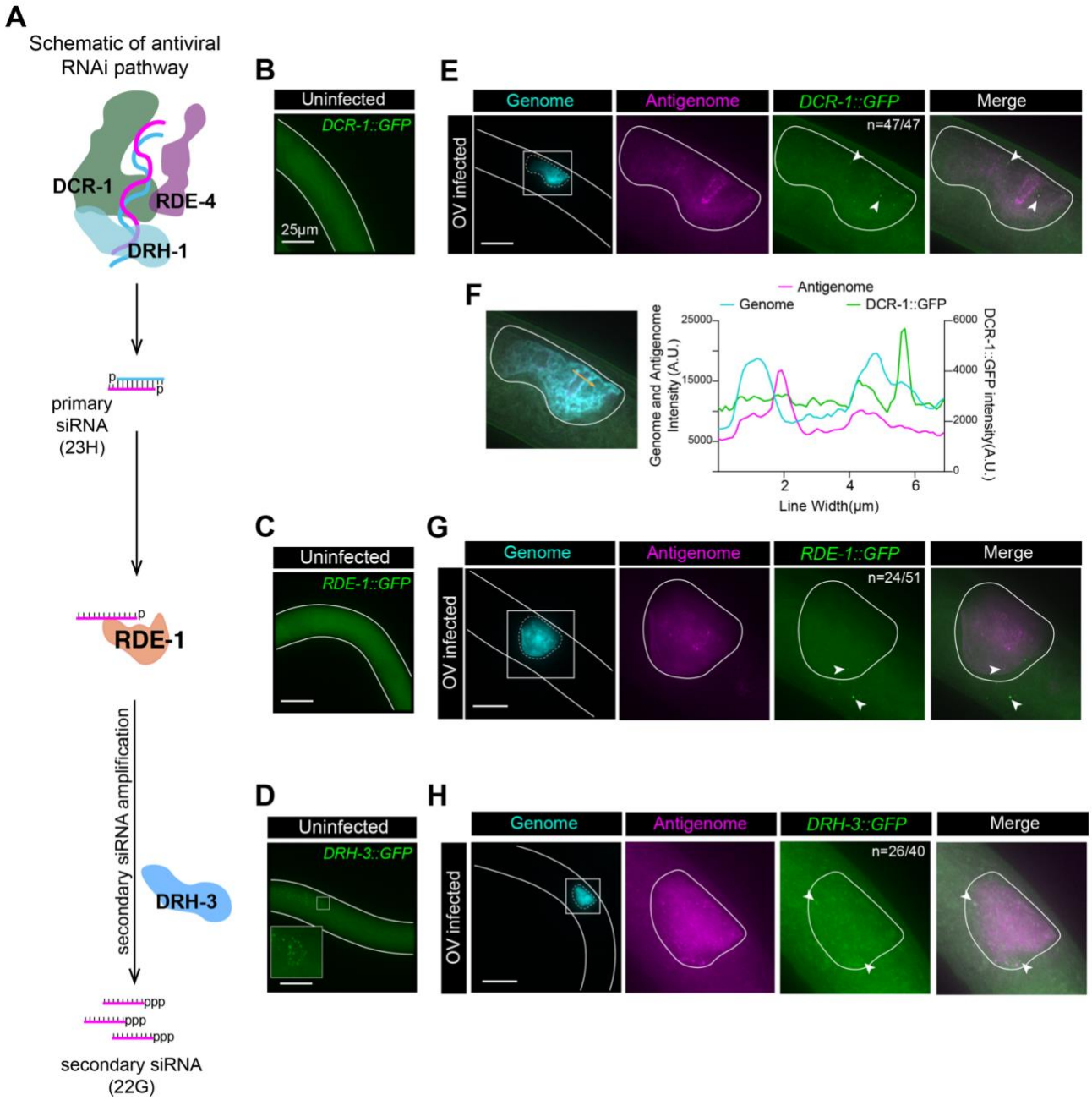
A
Schematic of antiviral RNAi pathway
DCR-1
RDE-4
DRH-1
primary siRNA (23H)
RDE-1
secondary siRNA amplification
DRH-3
secondary siRNA (22G)
B
Uninfected
DCR-1::GFP
25μm
C
Uninfected
RDE-1::GFP
D
Uninfected
DRH-3::GFP
E
Genome
Antigenome
DCR-1::GFP
Merge
OV infected
n=47/47
F
Antigenome
Genome
DCR-1::GFP
Genome and Antigenome Intensity (A.U.)
DCR-1::GFP intensity(A.U.)
Line Width(μm)
G
Genome
Antigenome
RDE-1::GFP
Merge
OV infected
n=24/51
H
Genome
Antigenome
DRH-3::GFP
Merge
OV infected
n=26/40

971

Fig 6

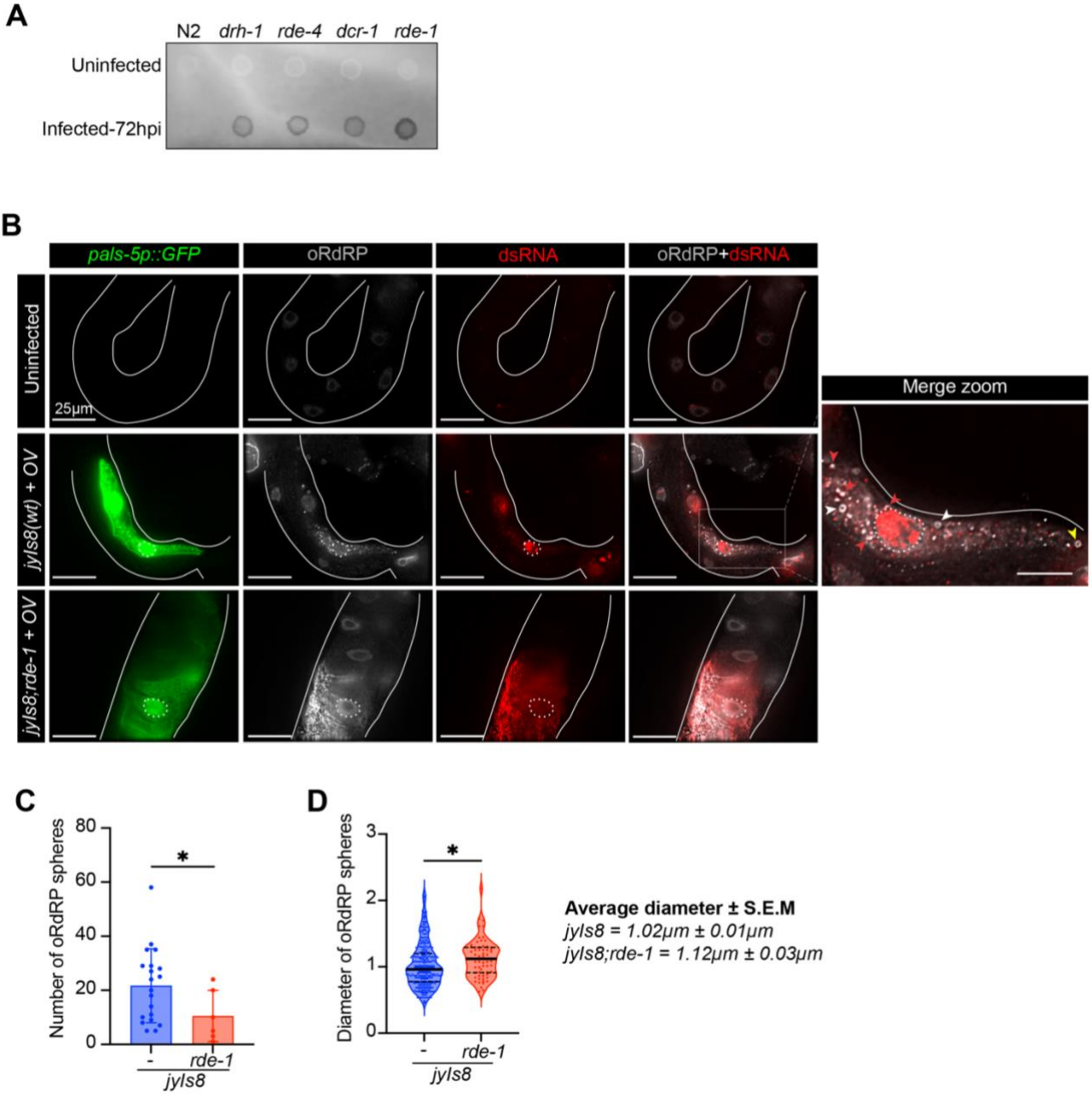
A
N2
drh-1
rde-4
dcr-1
rde-1
Uninfected
Infected-72hpi
B
pals-5p::GFP
oRdRP
dsRNA
oRdRP+dsRNA
Uninfected
25µm
jyIs8(wt) + OV
jyIs8;rde-1 + OV
Merge zoom
C
Number of oRdRP spheres
80
60
40
20
0
*
-
rde-1
jyIs8
D
Diameter of oRdRP spheres
3
2
1
0
*
-
rde-1
jyIs8
Average diameter ± S.E.M
jyIs8 = 1.02µm ± 0.01µm
jyIs8;rde-1 = 1.12µm ± 0.03µm

Fig 7

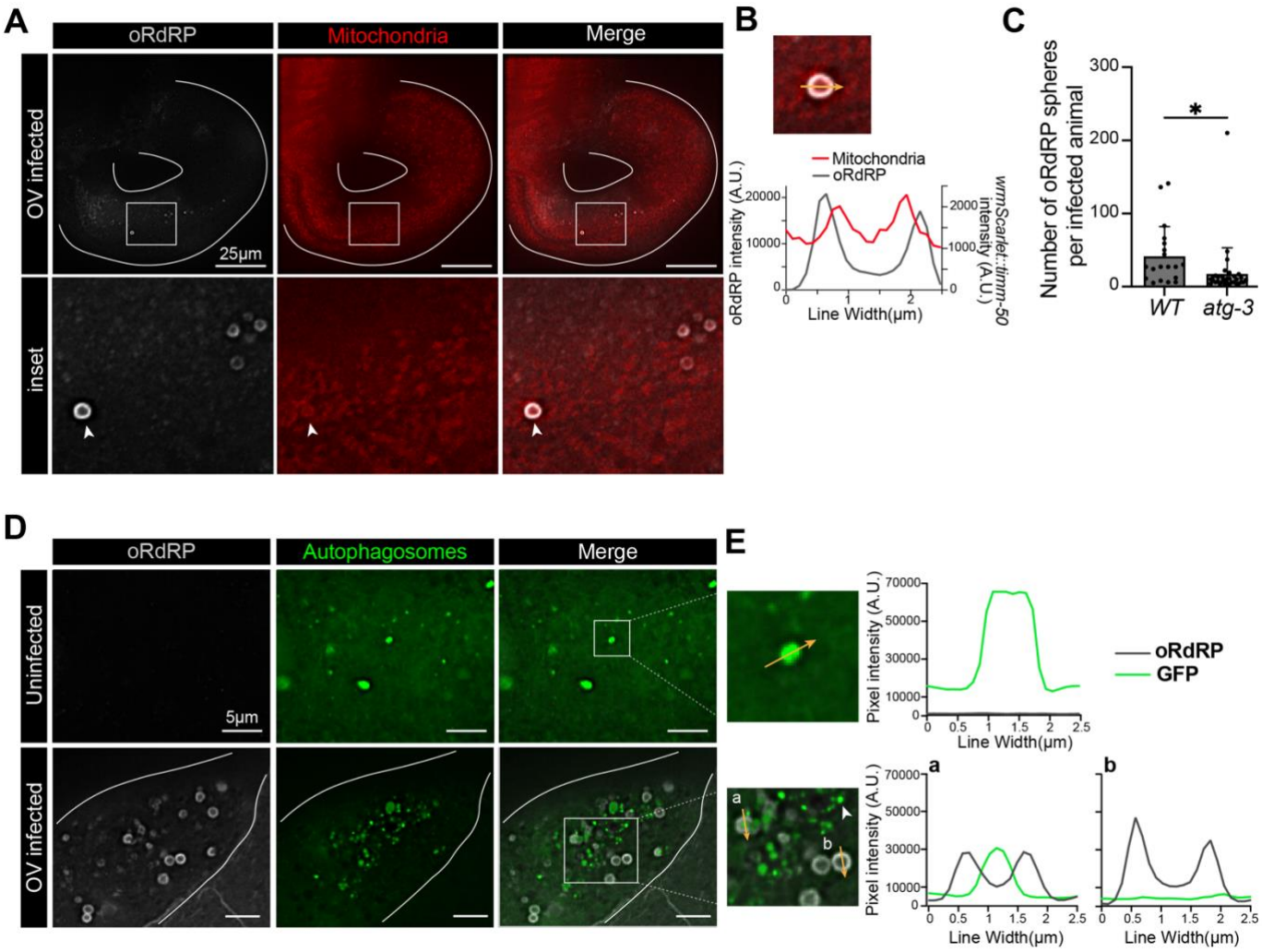
A
oRdRP
Mitochondria
Merge
OV infected
inset
25μm
B
Mitochondria
oRdRP
oRdRP intensity (A.U.)
wrmScarlet::tjmm-50 intensity (A.U.)
Line Width(μm)
C
Number of oRdRP spheres per infected animal
WT
atg-3
D
oRdRP
Autophagosomes
Merge
Uninfected
OV infected
5μm
E
Pixel intensity (A.U.)
Line Width(μm)
oRdRP
GFP
a
b

Fig 8

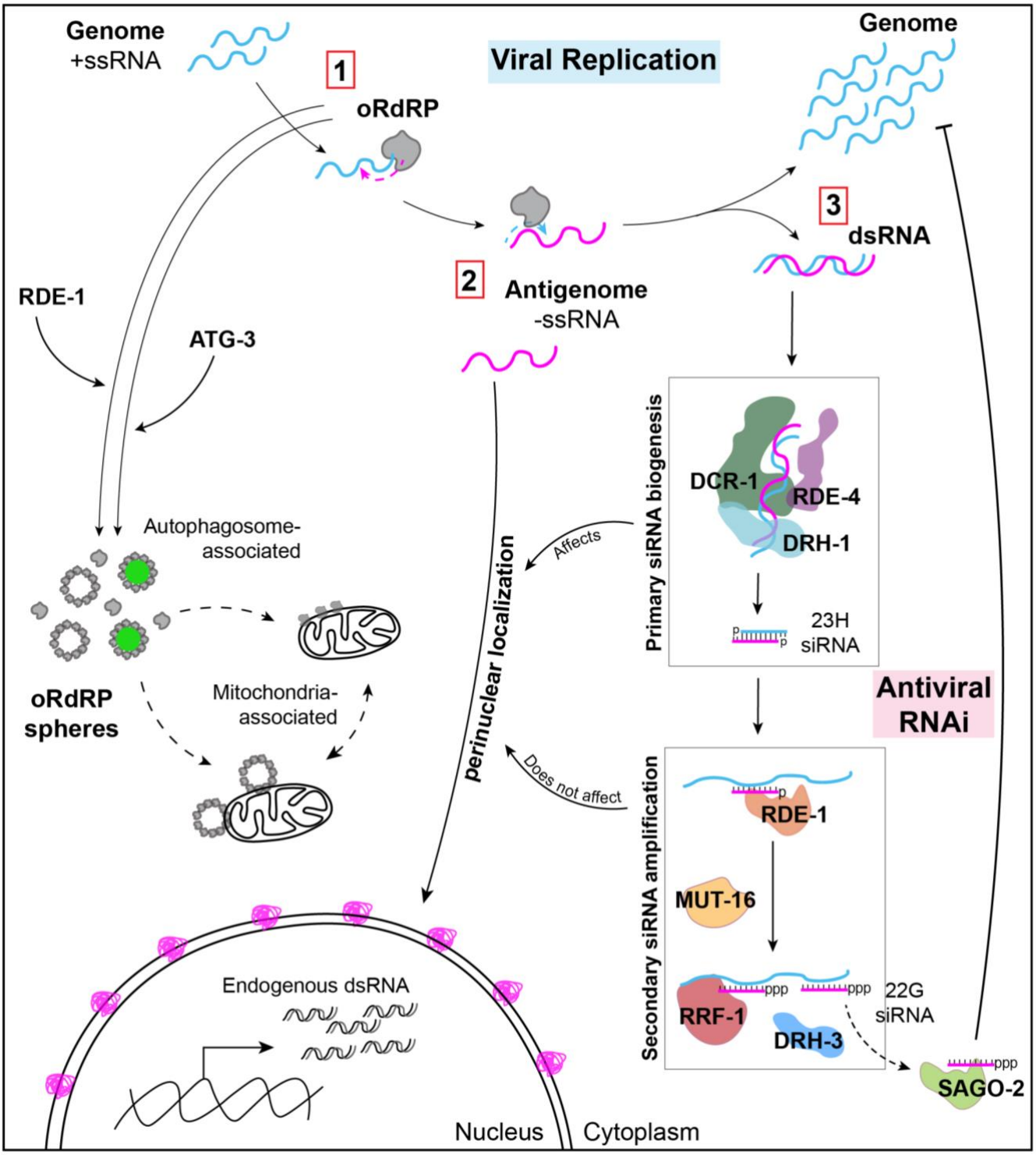
Genome
+ssRNA
Viral Replication
1
oRdRP
Genome
3
dsRNA
2
Antigenome
-ssRNA
RDE-1
ATG-3
Autophagosome-
associated
oRdRP
spheres
Mitochondria-
associated
perinuclear localization
Affects
Does not affect
Primary siRNA biogenesis
DCR-1
RDE-4
DRH-1
23H
siRNA
Antiviral
RNAi
Secondary siRNA amplification
RDE-1
MUT-16
RRF-1
DRH-3
22G
siRNA
SAGO-2
Endogenous dsRNA
Nucleus
Cytoplasm